Available online at www.sciencedirect.com
ScienceDirect
Comput. Methods Appl. Mech. Engrg. 361 (2020) 112752
Computer methods in applied mechanics and engineering
www.elsevier.com/locate/cma

An iterative staggered scheme for phase field brittle fracture propagation with stabilizing parameters

Mats Kirkesæther Brun[a,*], Thomas Wick[b], Inga Berre[a,c], Jan Martin Nordbotten[a], Florin Adrian Radu[a]

[a] *Department of Mathematics, University of Bergen, P.O. Box 7800, N-5020 Bergen, Norway*
[b] *Leibniz University Hannover, Institute of Applied Mathematics, AG Wissenschaftliches Rechnen, Welfengarten 1, 30167 Hannover, Germany*
[c] *NORCE Norwegian Research Centre AS, Bergen, Norway*

Received 21 March 2019; received in revised form 25 September 2019; accepted 11 November 2019
Available online 30 December 2019

Abstract

This paper concerns the analysis and implementation of a novel iterative staggered scheme for quasi-static brittle fracture propagation models, where the fracture evolution is tracked by a phase field variable. The model we consider is a two-field variational inequality system, with the phase field function and the elastic displacements of the solid material as independent variables. Using a penalization strategy, this variational inequality system is transformed into a variational equality system, which is the formulation we take as the starting point for our algorithmic developments. The proposed scheme involves a partitioning of this model into two subproblems; *phase field* and *mechanics*, with added stabilization terms to both subproblems for improved efficiency and robustness. We analyze the convergence of the proposed scheme using a fixed point argument, and find that under a natural condition, the elastic mechanical energy remains bounded, and, if the diffusive zone around crack surfaces is sufficiently thick, monotonic convergence is achieved. Finally, the proposed scheme is validated numerically with several bench-mark problems.

Keywords: Phase field; Fracture propagation; Iterative algorithm; Linearization; Convergence analysis; Finite element

1. Introduction

Fracture propagation is currently an important topic with many applications in various engineering fields. Specifically, phase-field descriptions are intensively investigated. The theory of brittle fracture mechanics goes back to the works of A. Griffith [1], wherein a criterion for crack propagation is formulated. Despite a foundational treatment on the subject of brittle fracture, Griffith's theory fails to predict crack initiation.

This deficiency can however be overcome by a variational approach, which was first proposed in [2,3]. Using such a variational approach, discontinuities in the displacement field u across the lower-dimensional crack surface are approximated by an auxiliary phase-field function φ. The latter can be viewed as an indicator function, which

* Corresponding author.
E-mail addresses: matskbrun@gmail.com (M. Kirkesæther Brun), thomas.wick@ifam.uni-hannover.de (T. Wick), inga.berre@uib.no (I. Berre), jan.nordbotten@uib.no (J.M. Nordbotten), florin.radu@uib.no (F.A. Radu).

https://doi.org/10.1016/j.cma.2019.112752

introduces a diffusive transition zone of size ε, the so-called length-scale parameter, between the broken and the unbroken material. The stress at which a crack nucleates, i.e. the cohesiveness of the phase-field model, depends on ε. In the sharp crack limit, a phase-field fracture would only nucleate from a stress singularity, corresponding to linear elastic fracture mechanics. The enforcement of irreversibility of crack growth finally yields a variational inequality system, of which we seek the solution $\{u, \varphi\}$.

In this work, we concentrate on improvements of the nonlinear solution algorithm, which is still a large bottleneck of phase-field fracture evolution problems. Specifically, high iteration numbers when the crack initiates or is further growing are reported in many works [4–7]. However, in most studies iteration numbers are omitted. Both staggered (splitting) schemes and monolithic schemes are frequently employed. Important developments include alternating minimization/staggered schemes [5,8–11], quasi-monolithic scheme with a partial linearization [12], and fully monolithic schemes [4,6,7].

The goal of this work is to propose a *linearized staggered scheme with stabilizing parameters*. In particular, the proposed scheme is based on recent developments on *iterative splitting schemes* coming from poroelasticity [13–16]. Iterative splitting schemes are widely applied to problems of coupled flow and mechanics, where at each iteration step either of the subproblems (i.e., flow or mechanics) is solved first, keeping some physical quantity constant (e.g., *fixed stress* or *fixed strain*), followed by solving the next subproblem with updated solution information. This procedure is then repeated until an accepted tolerance is reached. Further extensions of this technique involve tuning some artificial stabilization terms according to a derived contraction estimate in energy norms. Here, the quantity held constant during solving of the subproblems need not represent any physical quantity present in the model. This is the central idea in the so-called 'L-scheme', which has proven to perform robustly for Richards equation [17,18], for linear and nonlinear poroelasticity [19,20], and for nonlinear thermo-poroelasticity [21].

The L-scheme is a modified Newton method (or stabilized Picard), in which the Jacobi matrix is replaced by a diagonal matrix [17]. By this the robustness of this linearization method increases, the L-scheme is globally convergent, but the quadratic rate of convergence is lost. The L-scheme can also be combined with the Newton method, by computing first a few iterations with the L-scheme and then switching to Newton [17].

We propose here a variant of the L-scheme, adapted to phase field brittle fracture propagation models. This scheme is based on a partitioning of the model into two subproblems; *phase field* and *mechanics*. Here, the L-scheme acts both as a *stabilization* and as a *linearization*. Assuming that the mechanical elastic energy remains bounded during the iterations, and that the diffusive zone around crack surfaces is sufficiently thick, we give a proof of monotonic convergence of the proposed scheme by employing a fixed point argument.

The efficiency and robustness of the proposed scheme are demonstrated numerically with several bench-mark problems. Moreover, we compare the number of iterations needed for convergence with 'standard' staggered schemes (i.e., without stabilizing terms), and monolithic schemes in which the fully-coupled system is solved all-at-once. Furthermore, it is well known that when reaching the critical loading steps during the computation of brittle fracture phase field problems (i.e., when the crack is propagating), spikes in iteration numbers appear. For this reason, and thanks to the monotonic convergence property of the proposed scheme, we show that a (low) upper bound on the number of iterations may be enforced, while the computed results are still in very good agreement with the non-truncated solutions. Thus, using this 'truncated L-scheme', we effectively avoid the iteration spikes at the critical loading steps at the cost of negligible loss of accuracy. We mention that this strategy is not available with e.g. Newton iteration, as the iterate solutions may behave erratically for any number of iterations before finally converging. Moreover, the assumption that the mechanical elastic energy remains bounded during the iterations is verified numerically for all test cases.

The main aims of this work are three-fold: Under a natural assumption, we prove the convergence of a novel iterative staggered scheme, optimized for phase field brittle fracture propagation problems. Based on these theoretical findings, we design a robust solution algorithm with monotonic convergence properties. Finally, several numerical tests are presented in which our variants of the L-scheme are tested in detail.

The outline of this paper is as follows: In Section 2 we present the model equations and coefficients, in Section 3 we introduce the partitioned scheme and derive a convergence proof, in Section 4 we describe in detail our numerical algorithm in pseudo-code, and in Section 5 we provide several numerical experiments, in particular a *single edge notched tension test*, a *single edge notched shear test*, an *L-shaped panel test*, and a *asymmetrically notched three point bending test*. Finally, in Section 6 we provide some conclusions and summary of the work.

1.1. Preliminaries

In this section we explain the notation used throughout this article, see e.g. [22,23] for more details. Given an open and bounded set $B \subset \mathbb{R}^d$, $d \in \{2, 3\}$, and $1 \leq p < \infty$, let $L^p(B) = \{f : B \to \mathbb{R} : \int_B |f(x)|^p \mathrm{d}x < \infty\}$. For $p = \infty$, let $L^\infty(B) = \{f : B \to \mathbb{R} : \operatorname{ess\,sup}_{x\in B} |f(x)| < \infty\}$. In particular, $L^2(B)$ is the Hilbert space of square integrable functions with inner product $(\cdot, \cdot)$ and norm $\|f\| := (f, f)^{\frac{1}{2}}$. For $k \in \mathbb{N}$, $k \geq 0$, we denote by $W^{k,p}(B)$ the space of functions in $L^p(B)$ admitting weak derivatives up to k'th order. In particular, $H^1(B) := W^{1,2}(B)$ and we denote by $H^1_0(B)$ its zero trace subspace.

Note that we reserve the use of bold fonts for second order tensors. Hence, if $u, v \in L^2(B)$, their inner product is $(u, v) := \int_B u(x)v(x)\mathrm{d}x$, and similarly, if $u, v \in (L^2(B))^d$ then we take their inner product to be $(u, v) := \int_B u(x) \cdot v(x)\mathrm{d}x$. Finally, if $\mathbf{u}, \mathbf{v} \in (L^2(B))^{d\times d}$ then their inner product is $(\mathbf{u}, \mathbf{v}) := \int_B \mathbf{u}(x) : \mathbf{v}(x)\mathrm{d}x$.

We will also apply several classical inequalities, in particular: *Cauchy–Schwarz, Young, Poincaré*, and *Korn*. See e.g. [24,25] for a detailed description of these.

2. Governing equations

What follows is a brief description of the phase field approach for quasi-static brittle fracture propagation, see e.g. [3,11] for more details. Consider a (bounded open) polygonal domain $B \subset \mathbb{R}^d$, wherein $\mathcal{C} \subset \mathbb{R}^{d-1}$ denotes the fracture, and $\Omega \subset \mathbb{R}^d$ is the intact domain, and a time interval $(0, T)$ is given with final time $T > 0$. By introducing the phase field variable $\varphi : B \times (0, T) \to [0, 1]$, which takes the value 0 in the fracture, 1 in the intact domain, and varies smoothly from 0 to 1 in a transition zone of (half-)thickness $\varepsilon > 0$ around $\mathcal{C}$, the evolution of the fracture can be tracked in space and time. Using the phase field approach, the fracture $\mathcal{C}$ is approximated by $\Omega_F \subset \mathbb{R}^d$, where $\Omega_F := \{x \in \mathbb{R}^d : \varphi(x) < 1\}$.

Introducing the displacement vector $u : B\times(0, T) \to \mathbb{R}^d$, the model problem we consider arises as a minimization problem: An energy functional $E(u, \varphi)$ is defined according to Griffith's criterion for brittle fracture [1], which is then sought to be minimized over all admissible $\{u, \varphi\}$. From this minimization problem, the Euler–Lagrange equations are obtained by differentiation with respect to the arguments, yielding a variational equality system. Finally, a crack irreversibility condition must be enforced (the crack is not allowed to heal), which takes the form $\partial_t\varphi \leq 0$. Thus, the variational equality system, which is the previously mentioned Euler–Lagrange equations, is transformed into a variational inequality system, which reads as follows: Find $(u(t), \varphi(t)) \in V \times W := (H^1_0(B))^d \times W^{1,\infty}(B)$ such that for $t \in (0, T]$ there holds

$$(g(\varphi)\mathbb{C}\mathbf{e}(u), \mathbf{e}(v)) = (b, v), \ \forall v \in V, \tag{2.1a}$$

$$G_c\varepsilon(\nabla\varphi, \nabla\psi) - \frac{G_c}{\varepsilon}(1 - \varphi, \psi) + (1 - \kappa)(\varphi|\mathbb{C}\mathbf{e}(u)|^2, \psi) \geq 0, \qquad \forall\psi \in W, \tag{2.1b}$$

where $G_c > 0$ is the critical elastic energy restitution rate, $0 < \kappa \ll 1$ is a regularization parameter, the purpose of which is to avoid degeneracy of the elastic energy (equivalent with replacing the fracture with a softer material), and $g(\varphi) := (1 - \kappa)\varphi^2 + \kappa$ is the degradation function (which is a standard choice, see e.g. [7,26]. Note that $g(\varphi) \to \kappa$ when approaching the fracture zone). The body force acting on the domain B is $b : B \times (0, T) \to \mathbb{R}^d$, and $|\mathbb{C}\mathbf{e}(u)|^2 := \mathbb{C}\mathbf{e}(u) : \mathbf{e}(u)$ is the elastic mechanical energy, where $\mathbf{e}(\cdot) := (\nabla(\cdot) + \nabla(\cdot)^\top)/2$ is the symmetric gradient, and $\mathbb{C} = [C_{ijkl}]_{ijkl}$ is the fourth order tensor containing the elastic material coefficients, where each $C_{ijkl} \in L^\infty(B)$. We assume that $\mathbb{C}$ satisfies the usual *symmetry* and *positive definiteness* properties, i.e., $(\mathbb{C}\mathbf{u}, \mathbf{v}) = (\mathbf{u}, \mathbb{C}\mathbf{v})$, and $(\mathbb{C}\mathbf{u}, \mathbf{u})^{\frac{1}{2}}$ defines an L^2-equivalent norm, i.e., there exists constants $\lambda_m, \lambda_M > 0$ such that

$$\lambda_m\|\mathbf{u}\| \leq (\mathbb{C}\mathbf{u}, \mathbf{u})^{\frac{1}{2}} \leq \lambda_M\|\mathbf{u}\|, \qquad \text{for} \quad \mathbf{u}, \mathbf{v} \in (L^2(B))^{d\times d}, \ \mathbf{u}, \mathbf{v} \neq \mathbf{0}. \tag{2.2}$$

Note that due to the non-degeneracy of the elastic mechanical energy, the following estimate holds

$$\kappa \leq (\mathbb{C}\mathbf{e}(u), \mathbf{e}(u)). \tag{2.3}$$

In order to facilitate the following developments we assume continuity in time for $\{u, \varphi, b\}$. Let now $0 = t^0 < t^1 < \cdots < t^N = T$ be a partition of the time interval $(0, T)$, with time step $\delta t := t^n - t^{n-1}$, and denote the time discrete solutions by

$$u^n := u(\cdot, t^n), \tag{2.4}$$

$$\varphi^n := \varphi(\cdot, t^n). \tag{2.5}$$

The irreversibility condition now becomes $\varphi^n \leq \varphi^{n-1}$ (using a backward Euler method), and the time-discrete version of the problem (2.1a)–(2.1b) reads as follows: Find $(u^n, \varphi^n) \in V \times W$ such that

$$\big(g(\varphi^n)\mathbb{C}\mathbf{e}(u^n), \mathbf{e}(v)\big) = (b^n, v), \qquad \forall v \in V, \tag{2.6a}$$

$$G_c\varepsilon(\nabla\varphi^n, \nabla\psi) - \frac{G_c}{\varepsilon}(1-\varphi^n, \psi) + (1-\kappa)(\varphi^n|\mathbb{C}\mathbf{e}(u^n)|^2, \psi) + ([\Xi + \gamma(\varphi^n - \varphi^{n-1})]^+, \psi) = 0, \qquad \forall \psi \in W, \tag{2.6b}$$

where $b^n := b(\cdot, t^n)$. The last term in the phase field equation (2.6b) is a penalization to enforce the irreversibility condition, thus transforming the variational inequality (2.1b) into a variational equality, with penalization parameter $\gamma > 0$, and where $\Xi \in L^2(B)$ is given (in practice Ξ will be obtained by iteration, cf. Section 4). Note that we also used the notation $[x]^+ := \max(x, 0)$. From here on, we shall refer to (2.6a) as the *mechanics subproblem*, and to (2.6b) as the *phase field subproblem*. Regarding the degradation function g, it is easily seen to satisfy the following Lipschitz condition:

$$\|g(\psi) - g(\eta)\| \leq 2(1-\kappa)\|\psi - \eta\|, \quad \forall \psi, \eta \in W. \tag{2.7}$$

The time-discrete system (2.6a)–(2.6b) was analyzed in [27], and there it was shown that at least one global minimizer $(u^n, \varphi^n) \in V \times W$ exists, provided $b^n \in (L^2(B))^d$, for each n. We mention also that the analysis of a pressurized phase field brittle fracture model can be found in [28,29].

3. Iterative scheme

In this section we introduce the iterative staggered solution procedure for the fully discrete formulation of (2.6a)–(2.6b). To this end, let $\mathcal{T}_h$ be a simplicial mesh of B, such that for any two distinct elements of $\mathcal{T}_h$ their intersection is either an empty set or their common vertex or edge. We denote by h the largest diameter of all the elements in $\mathcal{T}_h$, i.e., $h := \max_{K\in\mathcal{T}_h} \mathrm{diam}(K)$, and let $V_h \times W_h \subset V \times W$ be appropriate (conforming) discrete spaces. We continue now with the same notation for the variables and test functions as before (omitting the usual h-subscript), since we will from here on mostly deal with the discrete solutions.

For each n, the iterative algorithm we propose defines a sequence $\{u^{n,i}, \varphi^{n,i}\}$, for $i \geq 0$, initialized by $\{u^{n-1}, \varphi^{n-1}\}$. The iteration is then done in two steps: First, the mechanics subproblem is solved, with the degradation function held constant. Then, the phase field subproblem is solved, with the elastic energy held constant. Note that there are also artificial stabilizing terms which are held constant during solving of the subproblems. Introducing the stabilization parameters $L_u, L_\varphi > 0$ (to be determined later), the iterative algorithm reads as follows:

- **Step 1** : Given $(u^{n,i-1}, \varphi^{n,i-1}, b^n)$ find $u^{n,i}$ such that

$$a_u(u^{n,i}, v) := L_u(u^{n,i} - u^{n,i-1}, v) + \big(g(\varphi^{n,i-1})\mathbb{C}\mathbf{e}(u^{n,i}), \mathbf{e}(v)\big) = (b^n, v), \qquad \forall v \in V_h. \tag{3.1a}$$

- **Step 2** : Given $(\varphi^{n,i-1}, u^{n,i}, \varphi^{n-1})$ find $\varphi^{n,i}$ such that

$$a_\varphi(\varphi^{n,i}, \psi) := L_\varphi(\varphi^{n,i} - \varphi^{n,i-1}, \psi) + G_c\varepsilon(\nabla\varphi^{n,i}, \nabla\psi) - \frac{G_c}{\varepsilon}(1-\varphi^{n,i}, \psi) + (1-\kappa)(\varphi^{n,i}|\mathbb{C}\mathbf{e}(u^{n,i})|^2, \psi) + (\eta^i(\Xi + \gamma(\varphi^{n,i} - \varphi^{n-1})), \psi) = 0, \qquad \forall \psi \in W_h, \tag{3.1b}$$

where, in order to avoid the $[\cdot]^+$-bracket, we also introduced the function $\eta^i \in L^\infty(B)$ defined for a.e. $x \in B$ by

$$\eta^i(x) = \begin{cases} 1, & \text{if } \Xi(x) + \gamma(\varphi^{n,i}(x) - \varphi^{n-1}(x)) \geq 0, \\ 0, & \text{if } \Xi(x) + \gamma(\varphi^{n,i}(x) - \varphi^{n-1}(x)) < 0. \end{cases} \tag{3.2}$$

3.1. Convergence analysis

We now proceed to analyze the convergence of the scheme (3.1a)–(3.1b). Our aim is to show a contraction of successive difference functions in energy norms, which implies convergence by the Banach Fixed Point Theorem (see e.g. [30]). To this end we define the following difference functions

$$e_u^i := u^{n,i} - u^n, \tag{3.3}$$

$$e_\varphi^i := \varphi^{n,i} - \varphi^n, \tag{3.4}$$

where $\{u^n, \varphi^n\}$ denotes the (exact) solutions to (2.1a)–(2.1b) at time t^n. Using the symmetry properties of $\mathbb{C}$, the following set of difference equations are then obtained by subtracting (3.1a)–(3.1b) solved by $\{u^n, \varphi^n\}$ from the same equations solved by the iterate solutions:

$$L_u(e_u^i - e_u^{i-1}, v) + (g(\varphi^n)\mathbb{C}\mathbf{e}(e_u^i), \mathbf{e}(v)) + ((g(\varphi^{n,i-1}) - g(\varphi^n))\mathbb{C}\mathbf{e}(u^{n,i}), \mathbf{e}(v)) = 0, \ \ \forall v \in V_h. \tag{3.5a}$$

$$\begin{aligned} L_\varphi(e_\varphi^i - e_\varphi^{i-1}, \psi) &+ G_c\varepsilon(\nabla e_\varphi^i, \nabla\psi) + \frac{G_c}{\varepsilon}(e_\varphi^i, \psi) + \gamma(\eta^i e_\varphi^i, \psi) \\ &+ (1-\kappa)(e_\varphi^i|\mathbb{C}\mathbf{e}(u^{n,i})|^2, \psi) \\ &+ (1-\kappa)\left(\varphi^n\mathbb{C}\mathbf{e}(e_u^i) : \mathbf{e}(u^{n,i} + u^n), \psi\right) = 0, \qquad \forall\psi \in W_h. \end{aligned} \tag{3.5b}$$

Furthermore, we introduce the following assumption related to the elastic mechanical strain.

Assumption 1 (*Boundedness of Elastic Strain*)**.** We assume there exists a constant $M > 0$ such that

$$\operatorname*{ess\,sup}_{x\in B} |\mathbf{e}(u^n(x))| \le M, \quad \forall n. \tag{3.6}$$

Moreover, we assume that M is large enough such that the above bound holds also for the iterate elastic strain, i.e.,

$$\operatorname*{ess\,sup}_{x\in B} |\mathbf{e}(u^{n,i}(x))| \le M, \quad \forall (n,i). \tag{3.7}$$

Note that M is nothing else than an upper bound for the elastic strain in the system for the converged solution, which is arguably finite for any reasonable problem. Note also that with sufficient regularity of the domain, coefficients, source terms, and initial data, the above assumption is satisfied, i.e., the problem (2.6a)–(2.6b) admits a solution $u^n \in (W^{1,\infty}(B))^d$, thus implying the existence of M. Alternatively to introducing the constant M, we could introduce instead a so-called 'cut-off operator' in the iterate equations (3.1a)–(3.1b), as seen in e.g. [31,32]. Note that in all numerical tests to be done in the next sections, we provide figures validating the second part of this assumption (cf. Section 5.5). With the above definitions, we state our main theoretical result.

Theorem 3.1 (*Convergence of the Scheme*)**.** *The scheme (3.1b)–(3.1a) defines a contraction satisfying*

$$\begin{aligned} &\left(\frac{L_\varphi}{2} + \frac{G_c}{\varepsilon} + \frac{G_c\varepsilon}{c_P} + \kappa(1-\kappa) - 8\xi^2\frac{(1-\kappa)^2}{\kappa}\right)\|e_\varphi^i\|^2 + \left(\frac{L_u}{2} + \frac{\kappa\lambda_{\min}^2}{4c_Pc_K}\right)\|e_u^i\|^2 \\ &\quad \le \frac{L_\varphi}{2}\|e_\varphi^{i-1}\|^2 + \frac{L_u}{2}\|e_u^{i-1}\|^2, \end{aligned} \tag{3.8}$$

if the stabilization parameters L_u and L_φ satisfy

$$L_u > 0, \quad L_\varphi \ge 16\xi^2(1-\kappa)^2/\kappa > 0, \tag{3.9}$$

and if the model parameter ε satisfies

$$\varepsilon > 0, \quad \varepsilon^2 - \frac{c_P}{G_c}\frac{1-\kappa}{\kappa}\left(8\xi^2(1-\kappa) - \kappa^2\right)\varepsilon + c_P > 0, \tag{3.10}$$

where $\xi := M\lambda_{\max}/\lambda_{\min} > 0$, and where $c_P, c_K > 0$ are the Poincaré and Korn constants, respectively, depending only on the domain B and spatial dimension d.

Proof. We begin by taking $v = e_u^i$ and $\psi = e_\varphi^i$ in (3.5a) and (3.5b), respectively, add the resulting equations together and obtain

$$\begin{aligned} &\left(\frac{L_\varphi}{2} + \frac{G_c}{\varepsilon}\right)\|e_\varphi^i\|^2 + \frac{L_\varphi}{2}\|e_\varphi^i - e_\varphi^{i-1}\|^2 + G_c\varepsilon\|\nabla e_\varphi^i\|^2 + \gamma(\eta^i e_\varphi^i, e_\varphi^i) \\ &\quad + (1-\kappa)(e_\varphi^i|\mathbb{C}\mathbf{e}(u^{n,i})|^2, e_\varphi^i) + \frac{L_u}{2}\|e_u^i\|^2 + \frac{L_u}{2}\|e_u^i - e_u^{i-1}\|^2 + (g(\varphi^n)\mathbb{C}\mathbf{e}(e_u^i), \mathbf{e}(e_u^i)) \\ &\quad = \frac{L_\varphi}{2}\|e_\varphi^{i-1}\|^2 + \frac{L_u}{2}\|e_u^{i-1}\|^2 - (1-\kappa)(\varphi^n\mathbb{C}\mathbf{e}(e_u^i) : \mathbf{e}(u^{n,i} + u^n), e_\varphi^i) \\ &\qquad - ((g(\varphi^{n,i-1}) - g(\varphi^n))\mathbb{C}\mathbf{e}(u^{n,i}), \mathbf{e}(e_u^i)), \end{aligned} \tag{3.11}$$

where we used the following inner product identity

$$2(z-y,z) = \|z\|^2 + \|z-y\|^2 - \|y\|^2. \tag{3.12}$$

Discarding some non-negative terms from the left hand side of (3.11), using the fact that $\operatorname{ess\,sup}_{x\in B}\varphi^n(x) \leq 1$, in addition to the Lipschitz property of the degradation function g (2.7), and non-degeneracy of the elastic energy (2.3) yields

$$\begin{aligned}
&\left(\frac{L_\varphi}{2} + \frac{G_c}{\varepsilon} + \kappa(1-\kappa)\right)\|e_\varphi^i\|^2 + \frac{L_\varphi}{2}\|e_\varphi^i - e_\varphi^{i-1}\|^2 + G_c\varepsilon\|\nabla e_\varphi^i\|^2 + \frac{L_u}{2}\|e_u^i\|^2 + \kappa(\mathbb{C}\mathbf{e}(e_u^i), \mathbf{e}(e_u^i)) \\
&\quad\leq \frac{L_\varphi}{2}\|e_\varphi^{i-1}\|^2 + \frac{L_u}{2}\|e_u^{i-1}\|^2 + (1-\kappa)\int_B |\mathbb{C}\mathbf{e}(e_u^i) : \mathbf{e}(u^{n,i}+u^n)e_\varphi^i|\mathrm{d}x \\
&\qquad + \int_B |(g(\varphi^{n,i-1}) - g(\varphi^n))\mathbb{C}\mathbf{e}(u^{n,i}) : \mathbf{e}(e_u^i)|\mathrm{d}x \\
&\qquad\quad\leq \frac{L_\varphi}{2}\|e_\varphi^{i-1}\|^2 + \frac{L_u}{2}\|e_u^{i-1}\|^2 + 2(1-\kappa)\lambda_{\max}M\Big(2\|e_\varphi^i\| + \|e_\varphi^i - e_\varphi^{i-1}\|\Big)\|\mathbf{e}(e_u^i)\|,
\end{aligned} \tag{3.13}$$

where we also invoked Assumption 1 in the last line, and applied the Cauchy–Schwarz and triangle inequalities. Using the Young inequality, the properties of elastic tensor (2.2), and rearranging, leads to

$$\begin{aligned}
&\left(\frac{L_\varphi}{2} + \frac{G_c}{\varepsilon} + \kappa(1-\kappa) - 4(1-\kappa)\lambda_{\max}M\frac{1}{2\delta_1}\right)\|e_\varphi^i\|^2 + G_c\varepsilon\|\nabla e_\varphi^i\|^2 \\
&\quad + \left(\frac{L_\varphi}{2} - 2(1-\kappa)\lambda_{\max}M\frac{1}{2\delta_2}\right)\|e_\varphi^i - e_\varphi^{i-1}\|^2 \\
&\quad + \frac{L_u}{2}\|e_u^i\|^2 + \Big(\kappa\lambda_{\min}^2 - (1-\kappa)\lambda_{\max}M(2\delta_1+\delta_2)\Big)\|\mathbf{e}(e_u^i)\|^2 \\
&\qquad\leq \frac{L_\varphi}{2}\|e_\varphi^{i-1}\|^2 + \frac{L_u}{2}\|e_u^{i-1}\|^2,
\end{aligned} \tag{3.14}$$

for some constants $\delta_1, \delta_2 > 0$. Choosing $\delta_1 = \kappa\lambda_{\min}^2/4(1-\kappa)\lambda_{\max}M$ and $\delta_2 = \kappa\lambda_{\min}^2/8(1-\kappa)\lambda_{\max}M$, and in addition demanding that

$$L_\varphi \geq 16M^2\frac{\lambda_{\max}^2}{\lambda_{\min}^2}\frac{(1-\kappa)^2}{\kappa}, \tag{3.15}$$

we can write (3.14) as

$$\begin{aligned}
&\left(\frac{L_\varphi}{2} + \frac{G_c}{\varepsilon} + \kappa(1-\kappa) - 8M^2\frac{\lambda_{\max}^2}{\lambda_{\min}^2}\frac{(1-\kappa)^2}{\kappa}\right)\|e_\varphi^i\|^2 + G_c\varepsilon\|\nabla e_\varphi^i\|^2 + \frac{L_u}{2}\|e_u^i\|^2 + \frac{\kappa\lambda_{\min}^2}{4}\|\mathbf{e}(e_u^i)\|^2 \\
&\qquad\leq \frac{L_\varphi}{2}\|e_\varphi^{i-1}\|^2 + \frac{L_u}{2}\|e_u^{i-1}\|^2.
\end{aligned} \tag{3.16}$$

Next, by applying the Poincaré inequality on $\|e_\varphi^i\|$, and by applying successively the Poincaré and Korn inequalities on $\|e_u^i\|$, we obtain

$$\|e_\varphi^i\|^2 \leq c_P\|\nabla e_\varphi^i\|^2 \quad \text{and} \quad \|e_u^i\|^2 \leq c_P c_K\|\mathbf{e}(e_u^i)\|^2, \tag{3.17}$$

where c_P, c_K are the (squares of the) Poincaré and Korn constants, respectively (depending only on the domain B and spatial dimension d). Finally, employing these bounds on the left hand side of (3.16), and defining the constant $\xi := M\lambda_{\max}/\lambda_{\min}$ yield

$$\begin{aligned}
&\left(\frac{L_\varphi}{2} + \frac{G_c}{\varepsilon} + \frac{G_c\varepsilon}{c_P} + \kappa(1-\kappa) - 8\xi^2\frac{(1-\kappa)^2}{\kappa}\right)\|e_\varphi^i\|^2 + \left(\frac{L_u}{2} + \frac{\kappa\lambda_{\min}^2}{4c_P c_K}\right)\|e_u^i\|^2 \\
&\qquad\leq \frac{L_\varphi}{2}\|e_\varphi^{i-1}\|^2 + \frac{L_u}{2}\|e_u^{i-1}\|^2.
\end{aligned} \tag{3.18}$$

Thus, for (3.18) to be a contraction estimate, ε must satisfy the following second order inequality

$$P(\varepsilon) := \varepsilon^2 - \frac{c_P}{G_c}\frac{1-\kappa}{\kappa}\left(8\xi^2(1-\kappa) - \kappa^2\right)\varepsilon + c_P > 0. \tag{3.19}$$

The range of admissible values for ε is then determined by the roots of the equation

$$P(\varepsilon) = 0, \tag{3.20}$$

which is given explicitly by

$$\varepsilon_{1,2} := \frac{1}{2}\frac{c_P}{G_c}\frac{1-\kappa}{\kappa}\left(8\xi^2(1-\kappa)-\kappa^2\right)\left(1 \pm \sqrt{1 - \frac{4G_c^2\kappa^2}{c_P(1-\kappa)^2(8\xi^2(1-\kappa)-\kappa^2)^2}}\right). \tag{3.21}$$

Since Eq. (3.20) is convex, and assuming $\varepsilon_{1,2}$ are real, the range of admissible values for ε is therefore given by

$$\varepsilon \in \Big((-\infty, \varepsilon_1) \cup (\varepsilon_2, \infty)\Big) \cap \mathbb{R}_{>0}. \tag{3.22}$$

In the case of $\varepsilon_1 = \varepsilon_2$, or in the case of $\varepsilon_{1,2}$ being complex, the inequality (3.19) holds true for all $\varepsilon > 0$. □

Remark 3.1 (*Convergence Rate*)**.** We note that due to some unknown constants (i.e. c_P, c_K and M) in the convergence rate (3.8), stabilization bounds (3.9) and constraint on ε (3.10), it is not known whether these estimates are optimal.

Remark 3.2 (*Constraint on* ε)**.** The above proof implies that the scheme is guaranteed to converge if $\varepsilon = \max\{\varepsilon_1, \varepsilon_2\}$ (for real valued roots of (3.20)), which is why we stated in the introduction that the proof of convergence holds if the diffusive zone around crack surfaces is sufficiently thick. Furthermore, working with a large ε is substantiated by the theory of phase field fracture being based on Γ convergence [33,34]. Applying this to phase field fracture was first done in [2]. Specifically, the setting is suitable when $h = o(\varepsilon)$; namely when ε is sufficiently large.

4. Algorithm

In practice, we apply the stabilizations and penalizations proposed in the previous sections as outlined below. It is well-known (e.g., [35]) that the choice of γ is critical. If γ is too low, crack irreversibility will not be enforced. On the other hand, if γ is too large, the linear equation system is ill-conditioned and influences the performance of the nonlinear solver. For this reason, γ is updated in at each iteration step. Better, in terms of robustness, is the augmentation in such an iteration by an additional L^2 function Ξ, yielding a so-called *augmented Lagrangian iteration* going back to [36,37]. For phase-field fracture this idea was first applied in [38]. Thus, combining the staggered iteration for the solid and phase-field systems with the update of the penalization parameter Ξ yields the following algorithm:

Algorithm 1.

At the loading step t^n.
Choose initial Ξ^0. *Set* $\gamma > 0$.
repeat
  Iterate on i (augmented Lagrangian loop)
  Solve two-field problem, namely
    Solve elasticity in Problem (3.1a)
    Solve the nonlinear phase-field in Problem (3.1b)
  Update

$$\Xi^{i+1} = [\Xi^i + \gamma(\varphi^{n,i+1} - \varphi^{n-1})]^+$$

until

$$\max(\|a_u(u^{n,i}, v_k) - (b^n, v_k)\|, \|a_\varphi(\varphi^{n,i}, \psi_l)\|) \leq \mathrm{TOL}, \tag{4.1}$$

$$\text{for } k = 1, \ldots, dim(V_h), \quad l = 1, \ldots, dim(W_h).$$

Set: $(u^n, \varphi^n) := (u^{n,i}, \varphi^{n,i})$.
Increment $t^n \to t^{n+1}$.

For the stabilization parameters L_u, L_φ, we have the following requirements (somewhat similar to γ): If the stabilization is too small, the stabilization effects vanish. If the stabilization is too large, we revert to an unacceptably slow convergence, and potentially, may converge to a solution corresponding to an undesirable local minimum of the original problem. In order to deal with these issues, we employ here a simple, yet effective strategy: We draw $L := L_u = L_\varphi$ from a range of suitable values and compare the results, i.e., $L \in \{1.0e{-}6, 1.0e{-}3, 1.0e{-}2, 1.0e{-}1\}$. Moreover, we include also for comparison the configurations $L_u = 0$, $L_\varphi > 0$ and $L_u = L_\varphi = 0$ in all the numerical tests to be done in the following.

Remark 4.1 (*Tolerance*)**.** In this paper we use $\text{TOL} = 10^{-6}$.

Remark 4.2 (*Penalization*)**.** Despite that we have carried out the convergence analysis and our algorithms using a penalization method to impose the crack irreversibility, our proposed stabilization is more general, and can be applied to other forms to imposing crack irreversibility (Dirichlet conditions, primal–dual active set, Lagrange multipliers; a list of currently used forms can be found in Chapter 7.2 in [39] and other discussions on the crack irreversibility constraint can be found in [40]) as well. The main reason is that the added stabilization terms in (3.1b) and (3.1a) are independent of the specific treatment of the variational inequality.

4.1. Nonlinear solution, linear subsolvers and programming code

Both subproblems (phase field and mechanics) may be nonlinear. In our theory presented above, we assumed a standard elasticity tensor. However, the model (3.1a)–(3.1b) is too simple for most mechanical applications. More realistic phase-field fracture applications require a splitting of the stress tensor (based on an energy split) in order to account for fracture development only under tension, but not under compressive forces. Consequently, we follow here [41] and split $\boldsymbol{\sigma}$ into tensile $\boldsymbol{\sigma}^+$ and compressive parts $\boldsymbol{\sigma}^-$:

$$\boldsymbol{\sigma}^+ := 2\mu_s \mathbf{e}^+ + \lambda_s \langle \text{tr}(\mathbf{e}) \rangle \mathbf{I},$$
$$\boldsymbol{\sigma}^- := 2\mu_s (\mathbf{e} - \mathbf{e}^+) + \lambda_s \big(\text{tr}(\mathbf{e}) - \langle \text{tr}(\mathbf{e}) \rangle \big) \mathbf{I},$$

and

$$\mathbf{e}^+ = \mathbf{P} \boldsymbol{\Lambda}^+ \mathbf{P}^T,$$

where the elasticity tensor $\mathbb{C}$ has been replaced by the Lamé parameters, μ_s and λ_s. Moreover, $\mathbf{I}$ is the $d \times d$ identity matrix, and $\langle \cdot \rangle$ is the positive part of a function. In particular, for $d = 2$, we have

$$\boldsymbol{\Lambda}^+ := \boldsymbol{\Lambda}^+(u) := \begin{pmatrix} \langle \lambda_1(u) \rangle & 0 \\ 0 & \langle \lambda_2(u) \rangle \end{pmatrix},$$

where $\lambda_1(u)$ and $\lambda_2(u)$ are the eigenvalues of the strain tensor $\mathbf{e} := \mathbf{e}(u)$, and $v_1(u)$ and $v_2(u)$ the corresponding (normalized) eigenvectors. Finally, the matrix $\mathbf{P}$ is defined as $\mathbf{P} := \mathbf{P}(u) := [v_1 | v_2]$; namely, it consists of the column vectors v_i, $i = 1, 2$. We notice that another frequently employed stress-splitting law was proposed in [42].

The modified scheme reads:

- **Step 1** : given $(u^{n,i-1}, \varphi^{n,i-1}, b^n)$ find $u^{n,i}$ such that

$$L_u(u^{n,i} - u^{n,i-1}, v) + \big(g(\varphi^{n,i-1}) \boldsymbol{\sigma}^+(u^{n,i}), \mathbf{e}(v) \big) + \big(\boldsymbol{\sigma}^-(u^{n,i}), \mathbf{e}(v) \big) = (b^n, v), \qquad \forall v \in V_h, \tag{4.2a}$$

- **Step 2** : given $(\varphi^{n,i-1}, u^{n,i}, \varphi^{n-1})$ find $\varphi^{n,i}$ such that

$$L_\varphi(\varphi^{n,i} - \varphi^{n,i-1}, \psi) + G_c \varepsilon(\nabla \varphi^{n,i}, \nabla \psi) - \frac{G_c}{\varepsilon}(1 - \varphi^{n,i}, \psi)$$
$$+ (1 - \kappa)(\varphi^{n,i} \boldsymbol{\sigma}^+(u^{n,i}) : \mathbf{e}(u^{n,i}), \psi) + (\eta^i(\Xi + \gamma(\varphi^{n,i} - \varphi^{n-1})), \psi) = 0, \qquad \forall \psi \in W_h. \tag{4.2b}$$

These modifications render the displacement system (4.2a) nonlinear, for which we use a Newton-type solver. The phase field equation is also nonlinear due to the penalization term and the stress splitting. Our version of Newton's method is based on a residual-based monotonicity criterion (e.g., [43]) outlined in [7][Section 3.2]. Inside Newton's method, the linear subsystems are solved with a direct solver; namely UMFPACK [44]. All numerical tests presented in Section 5 are implemented in the open-source finite element library deal.II [45,46]. Specifically, the code is based on a simple adaptation of the multiphysics template [47] in which specifically the previously mentioned Newton solver is implemented.

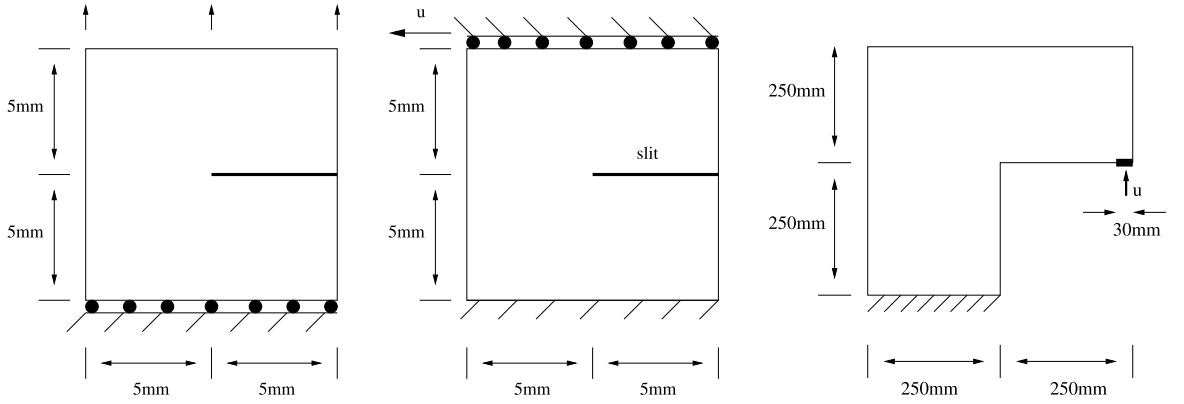

Fig. 1. Examples 1,2,3: Configurations. Left: single edge notched tension test. In detail, the boundary conditions are: $u_y = 0\,\text{mm}$ (homogeneous Dirichlet) and traction free (homogeneous Neumann conditions) in x-direction on the bottom. On the top boundary Γ_{top}, we prescribe $u_x = 0\,\text{mm}$ and u_y as provided in (5.3). All other boundaries including the slit are traction free (homogeneous Neumann conditions). Single edge notched shear test (middle) and L-shaped panel test (right). We prescribe the following conditions: On the left and right boundaries, $u_y = 0\,\text{mm}$ and traction-free in x-direction. On the bottom part, we use $u_x = u_y = 0\,\text{mm}$ and on Γ_{top}, we prescribe $u_y = 0\,\text{mm}$ and u_x as stated in (5.3). Finally, the lower part of the slit is fixed in y-direction, i.e., $u_y = 0\,\text{mm}$. For the L-shaped panel test (at right), the lower left boundary is fixed: $u_x = u_y = 0\,\text{mm}$. A displacement condition for u_y is prescribed by (5.4) in the right corner on a section Γ_u that has 30 mm length.

5. Numerical experiments

In this section, we present several numerical tests to substantiate our algorithmic developments. The goals of all three numerical examples are comparisons between an unlimited number of staggered iterations (although bounded by 500) denoted by 'L', and a low, fixed number, denoted by 'LFI', where we use 30 (Ex. 1 and Ex. 2), and 20 (Ex. 3 and Ex. 4) staggered iterations, respectively. These comparisons are performed in terms of the number of iterations and the correctness of the solutions in terms of the so-called *load–displacement curve*, measuring the forces of the top boundary versus the number of loading steps.

5.1. Single edge notched tension test

This test was applied for instance in [41]. The configuration is displayed in Fig. 1. We use the system (3.1a)–(3.1b). Specifically, we study our proposed iterative schemes on different mesh levels, denoted as refinement (Ref.) levels 4, 5, 6 (uniformly refined), with 1024 elements (2210 Dofs for the displacements, 1105 Dofs for the phase-field, $h = 0.044$), 4096 elements (8514 Dofs for the displacements, 4257 Dofs for the phase-field, $h = 0.022$), and 16 384 elements (33 410 Dofs for the displacements, 16 705 Dofs for the phase-field, $h = 0.011$).

Specifically, we use $\mu_s = 80.77\,\text{kN/mm}^2$, $\lambda_s = 121.15\,\text{kN/mm}^2$, and $G_c = 2.7\,\text{N/mm}$. The crack growth is driven by a non-homogeneous Dirichlet condition for the displacement field on Γ_{top}, the top boundary of B. We increase the displacement on Γ_{top} over time, namely we apply non-homogeneous Dirichlet conditions:

$$u_y = t\bar{u}, \quad \bar{u} = 1\,\text{mm/s}, \tag{5.1}$$

where t denotes the current loading time. Furthermore, we set $\kappa = 10^{-10}$ [mm] and $\varepsilon = 2h$ [mm]. We evaluate the surface load vector on the Γ_{top} as

$$\tau = (F_x, F_y) := \int_{\Gamma_{\text{top}}} \boldsymbol{\sigma}(u)\nu \, \mathrm{d}s, \tag{5.2}$$

with normal vector ν, and we are particularly interested in F_y for Example 1 and F_x for Example 2 (Section 5.2). Graphical solutions are displayed in Figs. 2 and 3 showing the phase-field variable and the discontinuous displacement field. Our findings of using different stabilization parameters L are compared in Figs. 4, 5, 6, 7, and 8. We have compared values of $L = L_u = L_{pf}$ ranging from $L = 0$, corresponding to no stabilization, and up to $L = 10^-2$. For all values of L, the iterative scheme converges, although there number of iterations depends

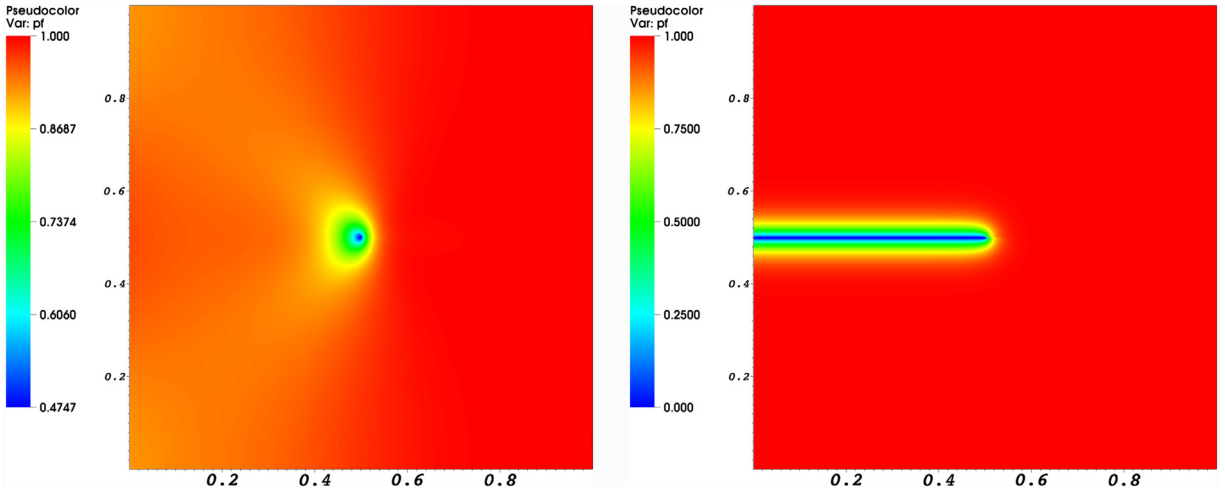

Fig. 2. Example 1: Single edge notched tension test: crack path at loading step 59 (left) and 60 (right). We see brutal crack growth in which the domain is cracked within one loading step.

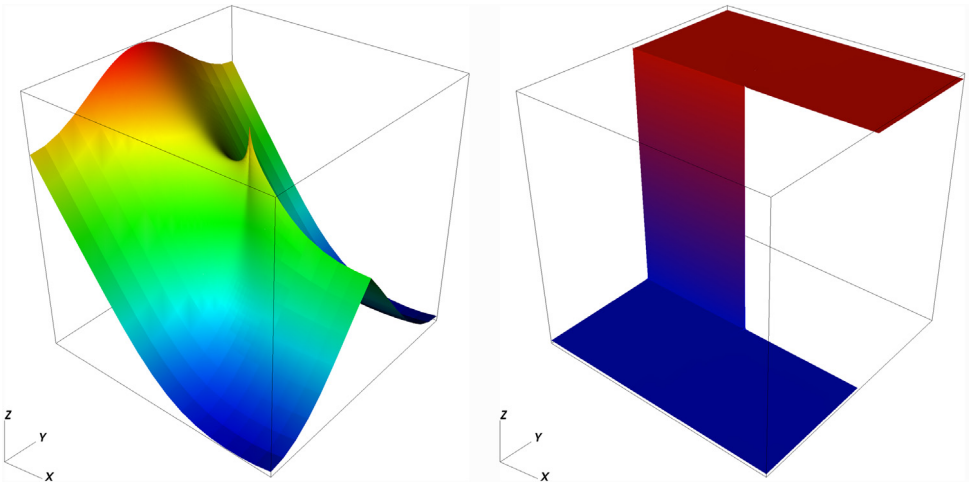

Fig. 3. Example 1: Single edge notched tension test: 3D plot of the displacement variable u_x at the loading steps 59 and 60. At right, the domain is totally fractured. In particular, we see the initial crack build in the geometry in the right part where the domain has a true discontinuity. In the left part, the domain is cracked using the phase-field variable. Here, the displacement variable is still continuous since we are using C^0 finite elements for the spatial discretization.

on L, as expected from the theory. Our results also demonstrate that the iteration is relatively robust with respect to stopping after a relatively modest number of iterations (30 in our examples), as only a minor loss of accuracy is observed. Moreover, in Fig. 5 we also include the stabilization configuration given by $L_u = 0$ but $L_\varphi > 0$. We note that Example 1 is the only one of our tests in which this particular configuration does not work (i.e., L_u cannot be arbitrarily small). This may be due to the very rapid crack growth occurring in this situation. Different mesh refinement studies are shown in Figs. 7 and 8. Here, the number of staggered iterations does not increase with finer mesh levels, which shows the robustness of our proposed methodology.

5.2. Single edge notched shear test

The configuration of this second setting is very similar to Example 1 and was first proposed in a phase-field context in [41]. We now use the model with strain–energy split (4.2a)–(4.2b). The parameters and the geometry

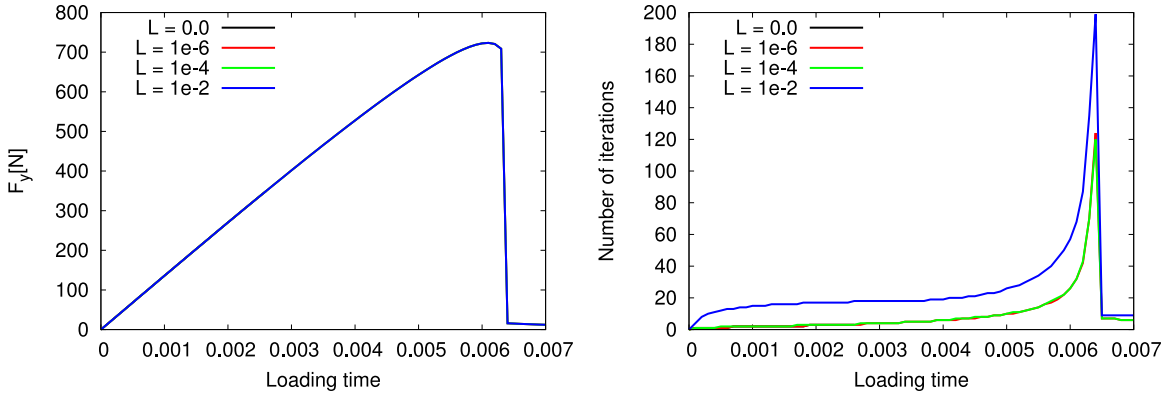

Fig. 4. Example 1: Comparison of different L. At left, the forces are shown. At right, the number of staggered iterations is displayed. We notice that in the left figure all curves are identical, indicating that our proposed numerical solution does not alter the physical solution. In the right figure, the black curve is hidden behind the red curve, which shows that for small L the number of iterations is not influenced.

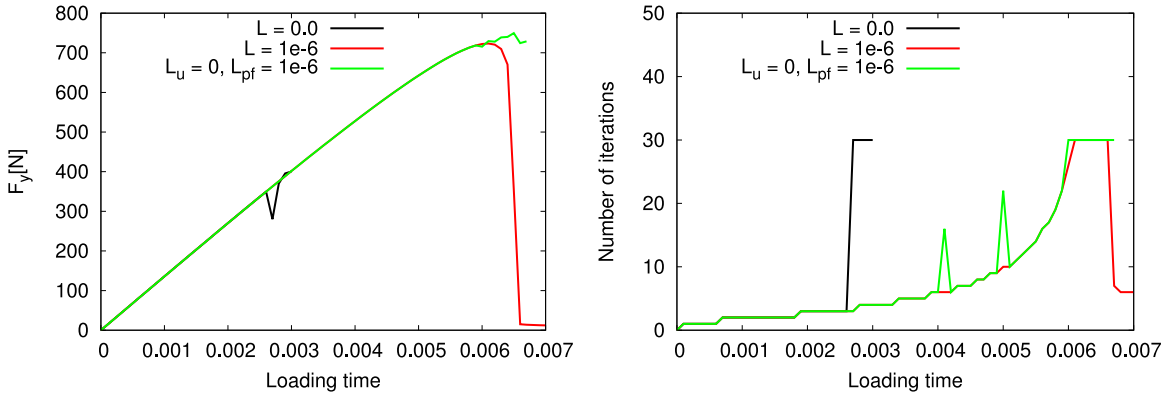

Fig. 5. Example 1: Comparison of different L for an upper bound of 30 iterations. At left the forces are shown. At right the number of iterations are displayed. In this example, possibly due to brutal crack growth, stabilizing only the phase field subproblem does not work. More specifically, the green and the black lines will not finish until the end time because the partitioned algorithm does diverge.

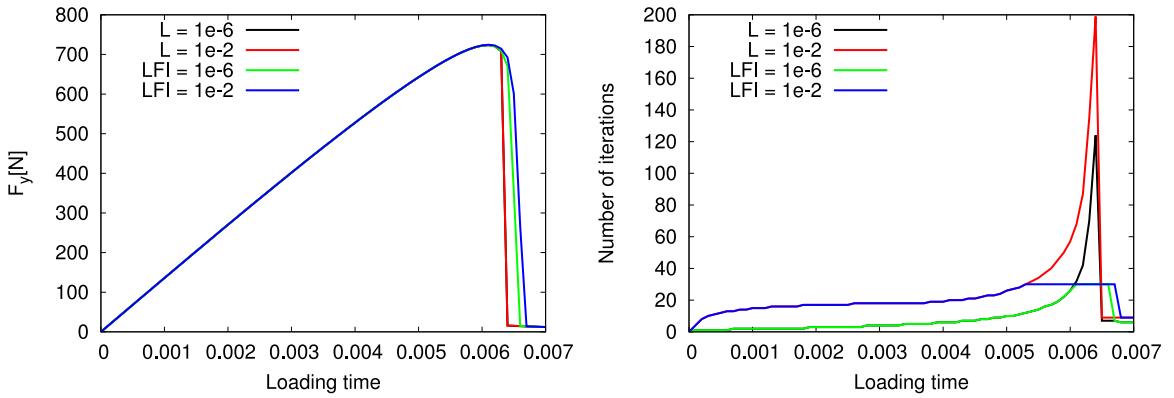

Fig. 6. Example 1: Comparison of different L for an open number of iterations and a fixed number of iterations (LFI) with a maximum of 30 iterations. At left, the forces are shown. At right, the number of staggered iterations is displayed.

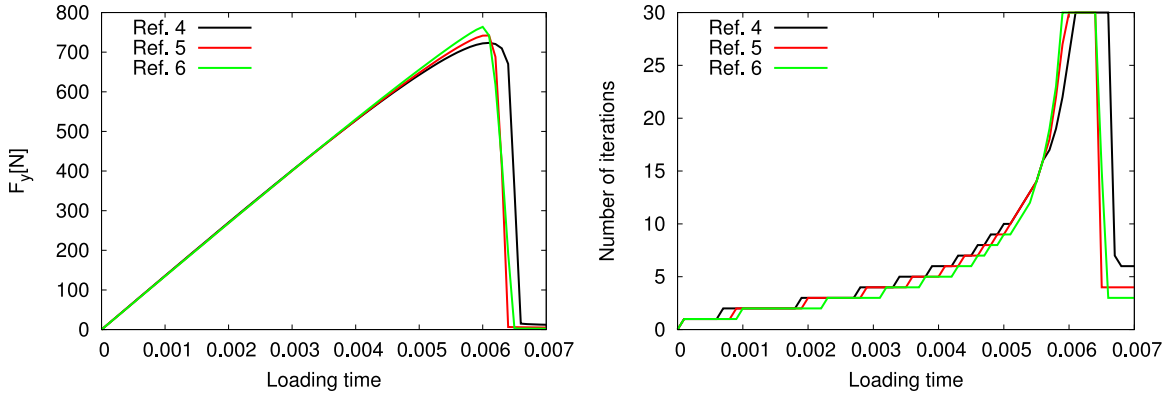

Fig. 7. Example 1: Using $L = 1e{-}6$ comparing different mesh refinement levels 4, 5, 6. At left, the forces are shown. At right, the number of staggered iterations is displayed.

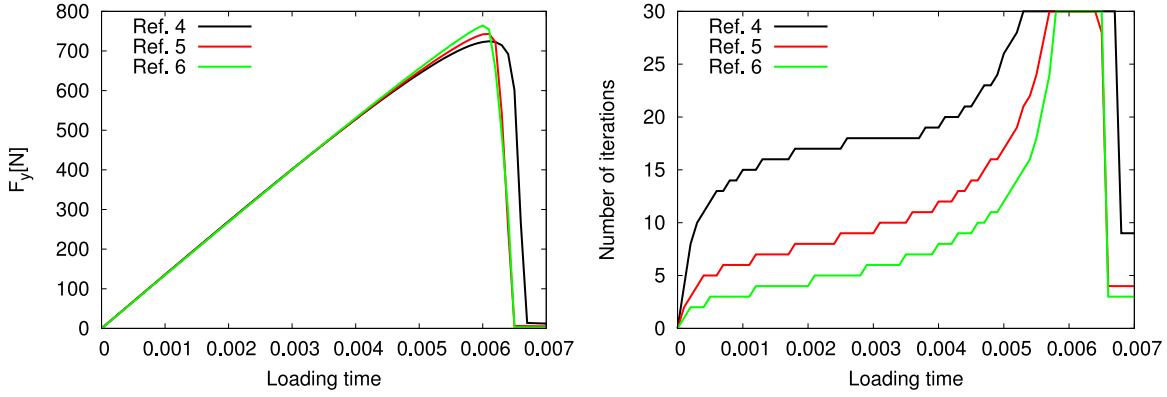

Fig. 8. Example 1: Using $L = 1e{-}2$ comparing different mesh refinement levels 4, 5, 6. At left, the forces are shown. At right, the number of staggered iterations is displayed.

(see Fig. 1) are the same as in the previous test case. The boundary condition is changed from tensile forces to a shear condition (see also again Fig. 1):

$$u_x = t\bar{u}, \quad \bar{u} = 1\,\text{mm/s}, \tag{5.3}$$

As quantity of interest we evaluate F_x in (5.2). Our findings are shown in the Figs. 9, 10, 11, 12, 13, 14, and 15.

As in Example 1, the load–displacement curves are very comparable to the published literature. In particular, it is nowadays known that the proposed Miehe et al. stress splitting [41] does not release all stresses once the specimen is broken (see [48]) and it is also known that we do not see convergence of the curves when both h and ε are refined (see [12]). Concentrating now more on the L-scheme, the proposed method is robust under mesh refinement (see Figs. 12–15). In these findings, it is important to notice that the accuracy of the simulation results is not affected whether a maximum of 500 iterations is allowed or the number of iterations is limited to 20; see Fig. 10. This indicates that the proposed scheme is not only robust, but also accurate. Since the crack grows more slower than in Example 1, also $L_u = 0$ works, as computationally justified in Fig. 11. In Fig. 11, the effect of the mechanics stabilization is studied by varying only L_u. Here, we see almost no influence. In Fig. 13, it can be observed that the number of L-iterations choosing $L = 1e{-}6$ and a maximum of 30 iterations is nearly independent of the mesh level, which is a very promising result. For $L = 1e{-}6$, the differences are slightly bigger, but the number of iterations even decreases under mesh refinement; see Fig. 15. We emphasize again that the accuracy of the numerical solution is, however, not affected.

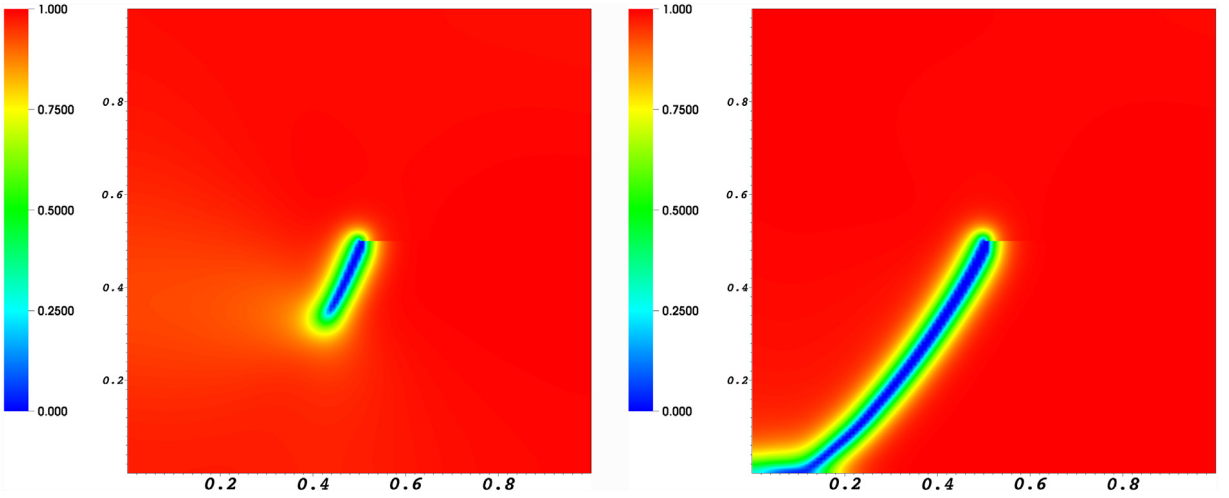

Fig. 9. Example 2: Single edge notched shear test: Crack path at loading step 110 (left) and 135 (right).

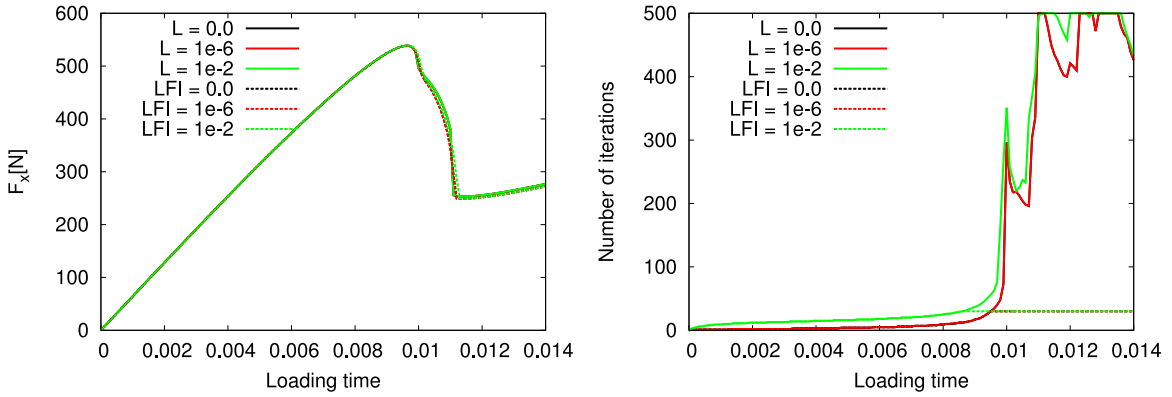

Fig. 10. Example 2: Comparison of different L with an open number of staggered iterations (fixed by 500) and a fixed number (LFI) with 30 iterations per loading step. At left, the load–displacement curves displaying the evolution of F_x versus the loading time. At right, the number of iterations is displayed.

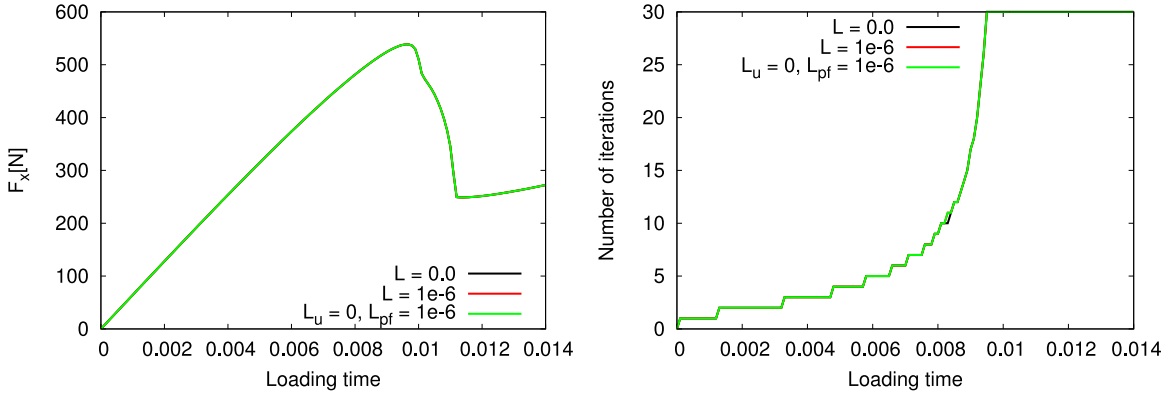

Fig. 11. Example 2: Comparison of different L. Observe that stabilizing the mechanics subproblem in this example has no or little effect. At left, the load–displacement curves displaying the evolution of F_x versus u_y are shown. At right, the number of staggered iterations is displayed.

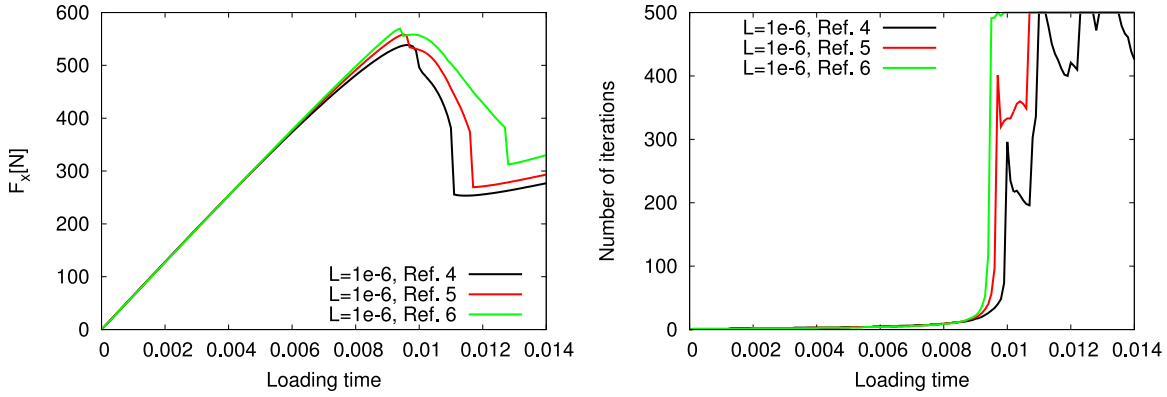

Fig. 12. Example 2: Using $L = 1e{-}6$, comparing different mesh refinement levels $4, 5, 6$. At left, the load–displacement curves displaying the evolution of F_x versus the loading time. At right, the number of iterations is displayed.

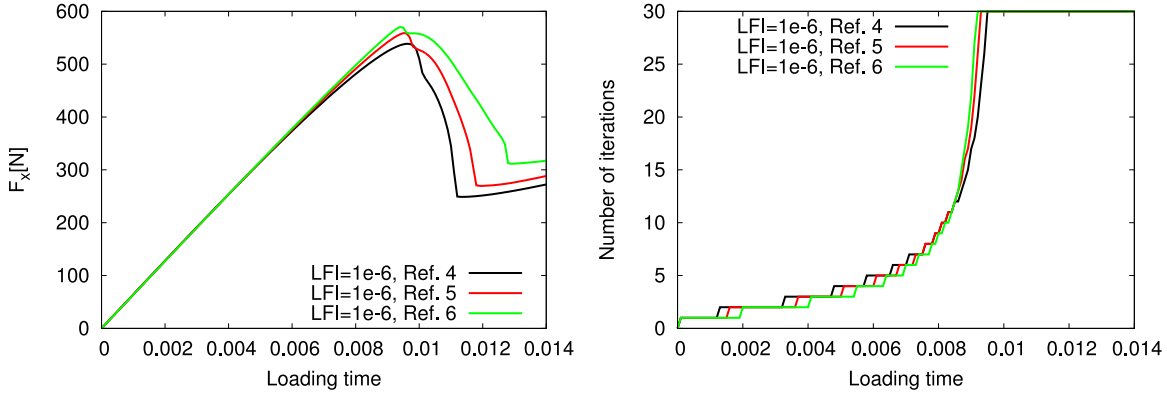

Fig. 13. Example 2: Using $L = 1e{-}6$ and fixing the number of iterations by 30, we compare different mesh refinement levels $4, 5, 6$. At left, the load–displacement curves displaying the evolution of F_x versus the loading time. At right, the number of iterations is displayed.

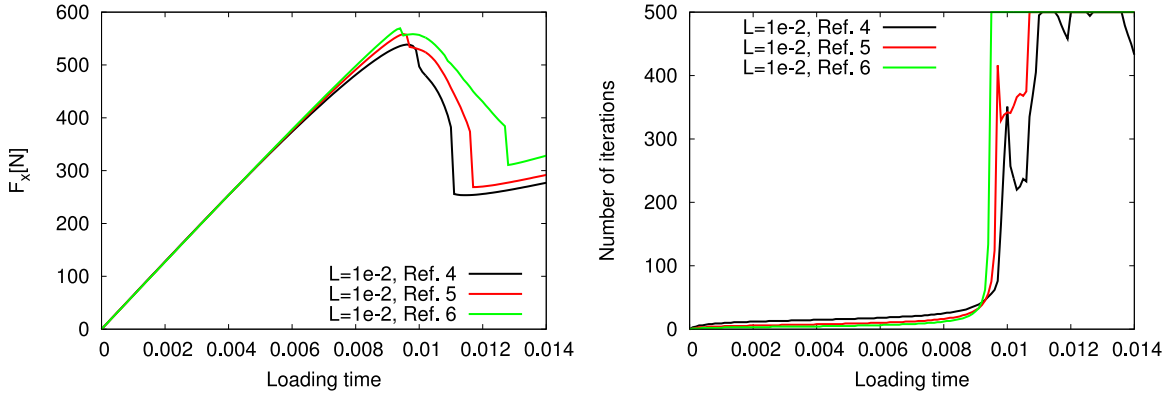

Fig. 14. Example 2: Using $L = 1e{-}2$, we compare different mesh refinement levels $4, 5, 6$. At left, the load–displacement curves displaying the evolution of F_x versus the loading time. At right, the number of iterations is displayed.

5.3. L-shaped panel test with monotonic loading

For the configuration of this third example we refer to [5,6,48], which are based on an experimental setup [49]. The exist basically two loading settings: the original one proposed in [49] with a monotonic loading and a cyclic

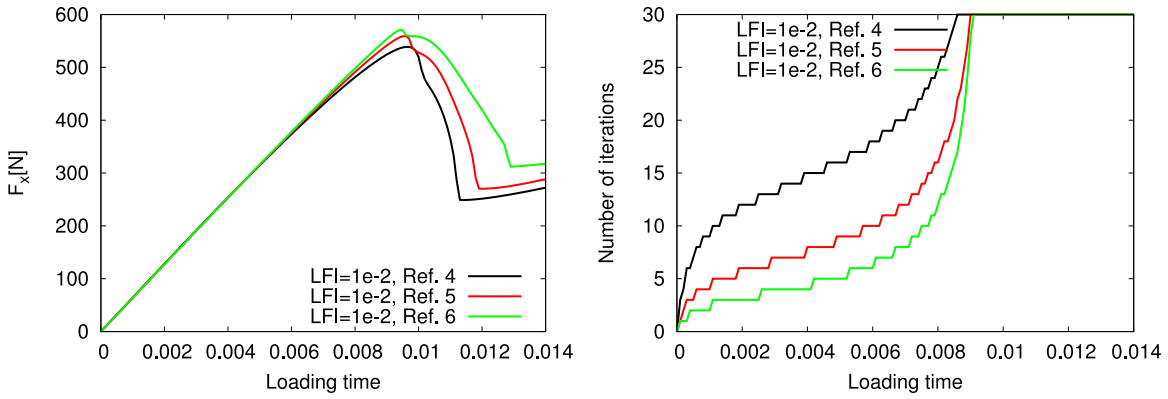

Fig. 15. Example 2: Using $L = 1e{-}2$ and fixing the number of iterations by 30, we compare different mesh refinement levels $4, 5, 6$. At left, the load–displacement curves displaying the evolution of F_x versus the loading time. At right, the number of iterations is displayed.

fashion proposed in [48]. Both were recently compared in [50]. We use again the model with strain–energy split; namely (4.2a)–(4.2b).

The geometry and boundary conditions are displayed in Fig. 1. In contrast to the previous examples, no initial crack prescribed. The initial mesh is 1, 2 and 3 times uniformly refined, leading to 300, 1200, 4800 mesh elements, with $h = 29.1548\,\text{mm}$, $14.577\,\text{mm}$, $7.289\,\text{mm}$, respectively.

We increase the displacement $u_D := u_y = u_y(t)$ on $\Gamma_u := \{(x, y) \in B \,|\, 470\,\text{mm} \leq x \leq 500\,\text{mm},\ y = 250\,\text{mm}\}$ over time, where Γ_u is a section of 30 mm length on the right corner of the specimen. We apply a loading-dependent, non-homogeneous Dirichlet condition:

$$u_y = t \cdot \bar{u}, \qquad \bar{u} = 1\,\text{mm/s}, \quad 0.0\,\text{s} \leq t < 0.8\,\text{s}, \tag{5.4}$$

where t denotes the total loading time. The total number of loading steps is 800.

We set (see [5]) Young's modulus $E = 25.85\,\text{GPa}$, Poisson's ratio $\nu = 0.18$, and the critical energy release $G_c = 95\,\text{N/m}$. The time (loading) step size is $\delta t = 10^{-3}\,\text{s}$. Furthermore, we set $k = 10^{-10}h$ [mm] and $\varepsilon = 2h$. As before, we observe the number of Newton iterations and we evaluate the surface load vector on $\Gamma_{\text{bottom}} := \{(x, y) \in B \,|\, 0\,\text{mm} \leq x \leq 250\,\text{mm},\ y = 0\,\text{mm}\}$ as

$$\tau = (F_x, F_y) := \int_{\Gamma_{\text{bottom}}} \boldsymbol{\sigma}(u)\nu \,\mathrm{d}s,$$

with normal vector ν, and now we are particularly interested in F_y. The crack path displayed in Fig. 16 corresponds to the literature values; see e.g., [5] or [50]. Our findings with respect to the L-scheme are as follows: Under mesh refinement, we observe the usual discretization error as in Example 1 and 2; see Fig. 17. In Fig. 18, we summarize our findings using a maximum of 20 or 500 iterations and various values for the stabilization parameters. Most importantly, the numerical solution, here evaluated in terms of the force at Γ_{bottom} is not influenced (left subfigure of Fig. 18). The corresponding number of iterations are displayed in the right subfigure of Fig. 18, highlighting that the maximum number of iterations is taken from $t = 0.22$ on and resulting in a much higher computational cost. These results confirm our findings from Example 2.

5.4. An asymmetrically notched three point bending test

In the fourth numerical example, we address an asymmetric three point bending test, which was previously considered by others as well [5,41,48] and was originally inspired by numerical and experimental setups from [51].

The configuration including geometry data (in mm) is shown Fig. 19. The specimen is deformed using a smoothly-in-space displacement on the entire top boundary Γ_{top}:

$$u(t, x, y = 8) = -10.0 * t * \exp(-(x - 10.0)^2/100).$$

As before, $t = 10^{-3} \sum_i^{20} i$ denotes the loading parameter and in total we compute 20 loading steps.

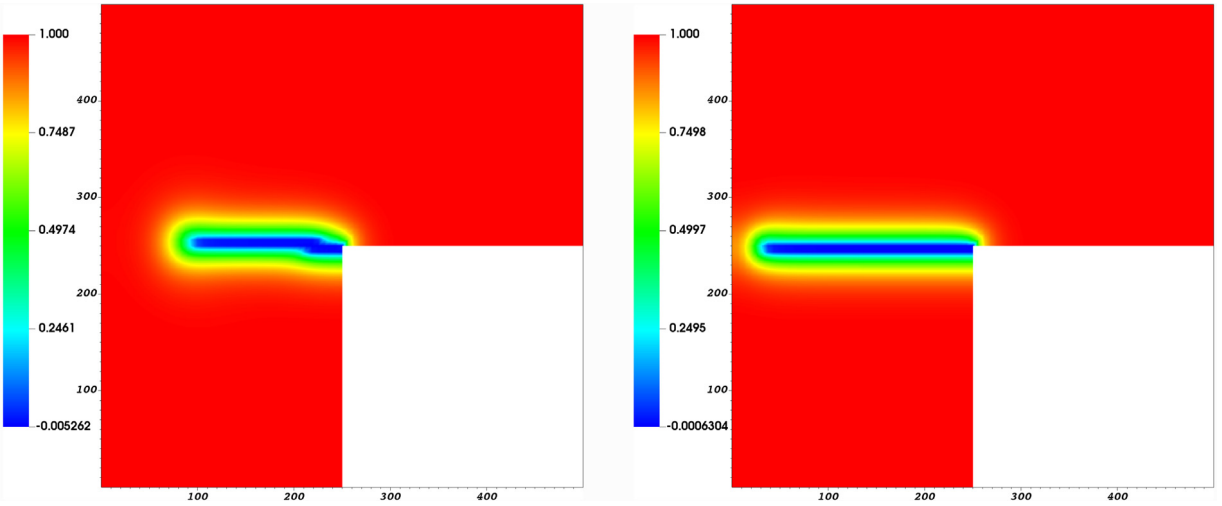

Fig. 16. Example 3: crack path of the L-shaped panel test at the loading steps 400 and 800.

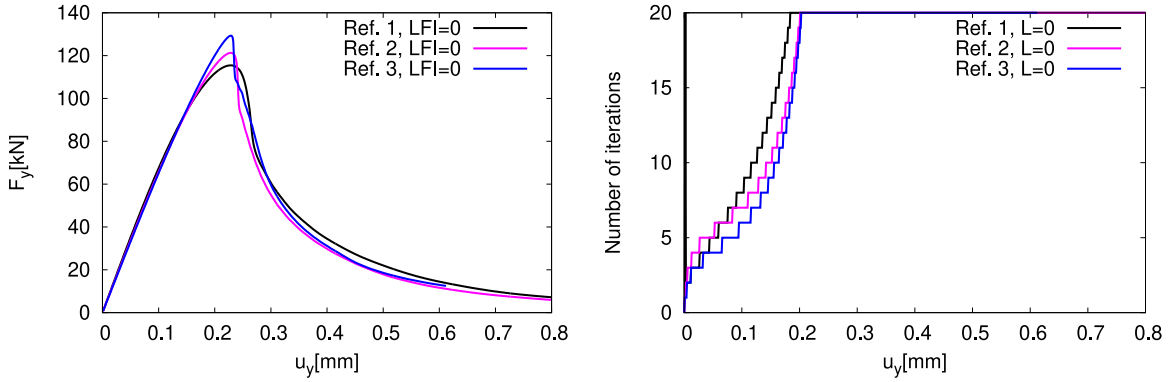

Fig. 17. Example 3: L-shaped panel test on different refinement levels and using the truncated iteration with a maximum of 20 iterations.

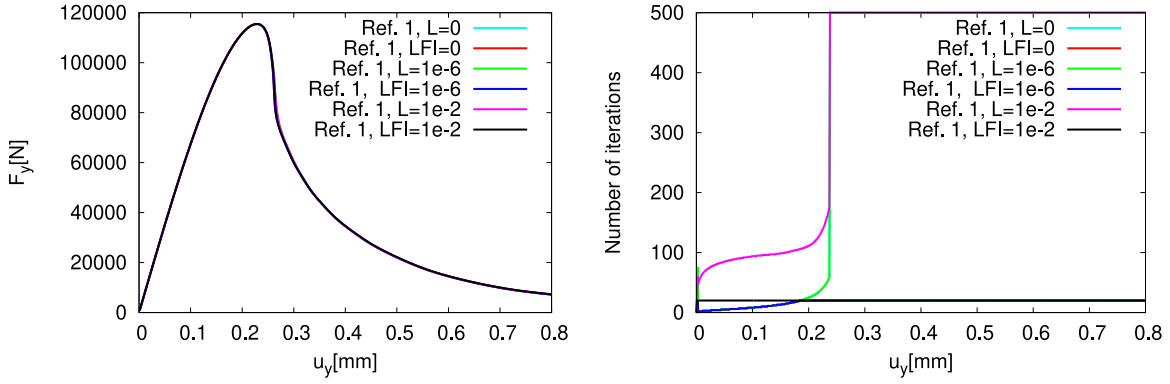

Fig. 18. Example 3: Comparison of various choices for the stabilization parameter L and the truncated iteration and the iteration with a maximum of 500 steps.

The choice was made in order to avoid a mathematically ill-posed setting by using a 'true' point displacement. As explained in [5], in the most left and right parts of the domain, the phase-field variable is fixed to $\varphi = 1$ in order to avoid artificially-induced cracks due to the loading and the boundary conditions.

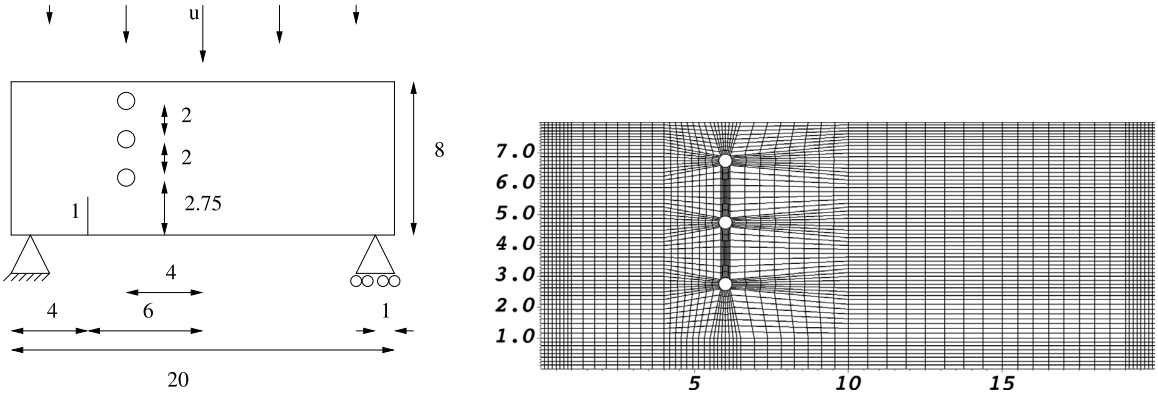

Fig. 19. Example 4: Asymmetric notched three point bending test. The geometry, loading and boundary conditions are taken from [51]. The three holes have each a diameter of 0.5. All units are in mm. At right, the three times uniformly refined mesh is displayed.

The initial mesh is 3, 4 and 5 times uniformly refined yielding 3904, 15 616 and 62 464 mesh elements with the minimal mesh size parameter $h_3 = 0.135$, $h_4 = 0.066$ and $h_5 = 0.033$.

As material parameters, we use $\mu_s = 8\,\mathrm{kN/mm^2}$, $\lambda_s = 12\,\mathrm{kN/mm^2}$, and $G_c = 1 \times 10^{-3}\,\mathrm{kN/mm}$. Furthermore, we set $k = 10^{-10}h$ [mm] and $\varepsilon = 2h$.

In our numerical simulations, we find that our formulation can also deal with more complex crack propagation problems. However, as also discussed in [41], the mesh must be sufficiently fine such that the crack reaches the second hole and not the first one (Fig. 20). The forces on the top boundary and the number of iterations are shown in the Figs. 21, 22, and 23. Overall, we can say that the proposed scheme works again well. However, the simulations with $L = 0$ show very competitive behaviors in comparison to $L > 0$. On the other hand, if L is too big (here we choose $L = 1$, the stabilization terms alter the physical model and the final (physical) numerical results are wrong; namely the crack will start propagating too late.

5.5. *Verification of Assumption 1*

In this last set of computations, we verify whether Assumption 1 holds true in our computations. We choose some prototype settings, namely on mesh refinement level 4 (Examples 1 and 2), and level 3 (Example 3), and level 5 (Example 4) and $L_u = L_\varphi = 1e{-}6$ (Example 1,2,3) and $L_u = L_\varphi = 1e{-}2$. In Fig. 24, we observe that $\operatorname{ess\,sup}_{x\in B} |\mathbf{e}(u^n(x))|$ varies, but always can be bounded from above with $M > 0$. The value of $\operatorname{ess\,sup}_{x\in B} |\mathbf{e}(u^n(x))|$ is the final strain when the L-scheme terminates. The minimum and maximum values show that there are no significant variations in $\operatorname{ess\,sup}_{x\in B} |\mathbf{e}(u^n(x))|$ during the L-scheme iterations with respect to the finally obtained value.

6. Conclusions

We have proposed a novel staggered iterative algorithm for brittle fracture phase field models. This algorithm is employing stabilization and linearization techniques known in the literature as the 'L-scheme', which is a generalization of the Fixed Stress Splitting algorithm coming from poroelasticity. Through theory and numerical examples we have investigated the performance of our proposed variants of the L-scheme for brittle fracture phase field problems.

Under natural constraints that the elastic mechanical energy remains bounded, and that the model parameter ε is sufficiently large (i.e., that the diffusive zone around crack surfaces must be sufficiently thick), we have shown that a contraction of successive difference functions in energy norms can be obtained from the proposed scheme. This result implies the algorithm is converging monotonically with a linear convergence rate. However, in the convergence analysis there appears some unknown constants which makes the precise convergence rate, as well as the precise lower bounds on ε and L_φ unknown.

We provide detailed numerical tests (including a challenging test such as Example 4 with an asymmetrically notched three point bending setting) where our proposed scheme is employed on several phase field brittle

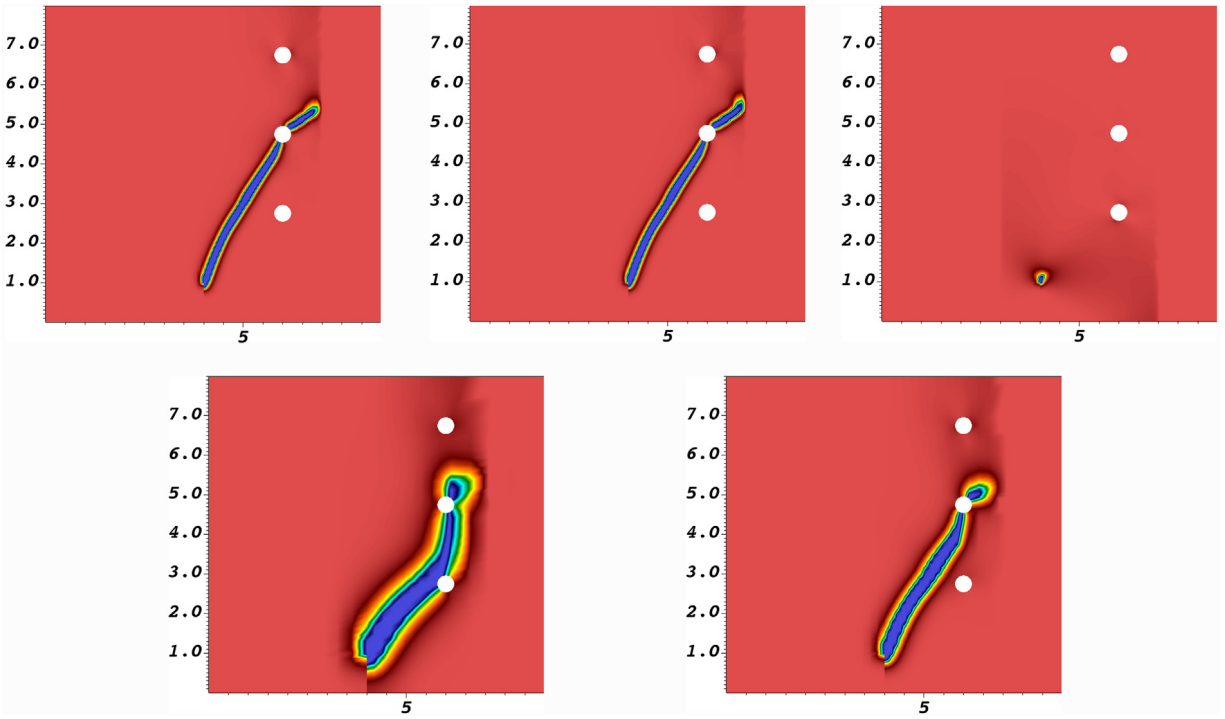

Fig. 20. Example 4: crack path of the asymmetric three point bending test when the second hole is reached. Top row: crack path after 20 loading steps for $L = 0, 1e{-}2, 1$ with mesh refinement 5. Bottom row: fixing $L = 1e{-}2$ and observing the mesh refinement levels 3 and 4. Mesh refinement level 5 is the middle figure in the top row. We see (top row) that $L = 1$ influences the numerical solution such that the crack does not yet grow after 20 loading steps. If the mesh is too coarse (bottom row), the crack first reaches the first hole. This has also been observed and discussed in [41].

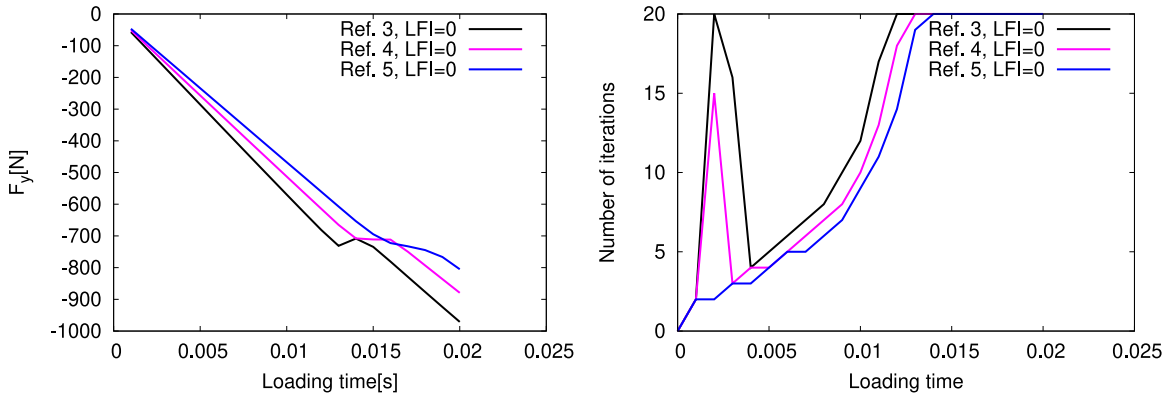

Fig. 21. Example 4: Comparison of the forces (left) over the top boundary and the number iterations for the truncated scheme without stabilization.

fracture bench-mark problems. For each numerical example we provide findings for different values of stabilization parameters. For most cases we let $L_u = L_\varphi > 0$, but for comparison we include also for the stabilization configurations $L_u = 0$ with $L_\varphi > 0$, and $L_u = L_\varphi = 0$. For the test cases presented here, there is only Example 1 where $L_u = 0$ does not work. This might be due to the very rapid crack growth, which sets Example 1 apart from Examples 2 and 3. In this regard, we conclude that further work is needed to find an optimal configuration of L_u and L_φ. For all numerical test we also provide computational justification for the assumption of bounded elastic mechanical energy. Furthermore, a slight dependency on h in the iteration counts is observed in the numerical tests,

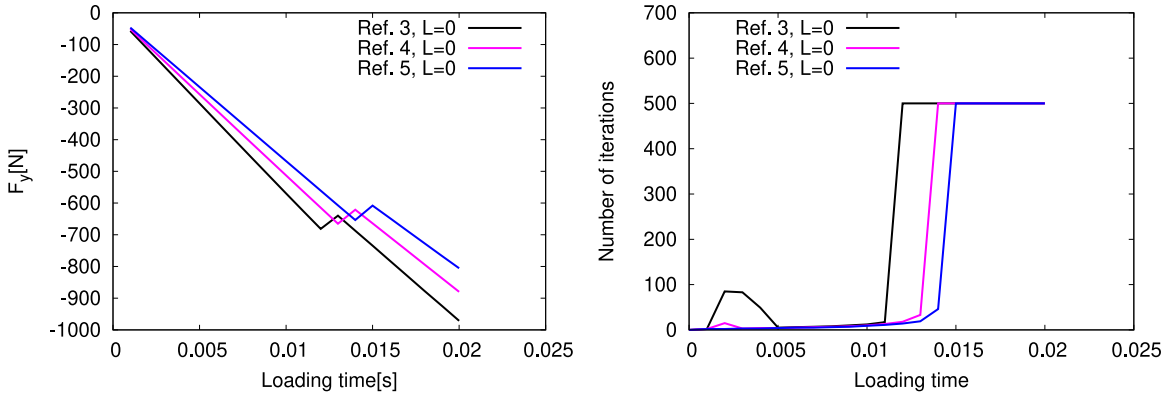

Fig. 22. Example 4: Comparison of the forces (left) over the top boundary and the number iterations (maximum of 500) without stabilization.

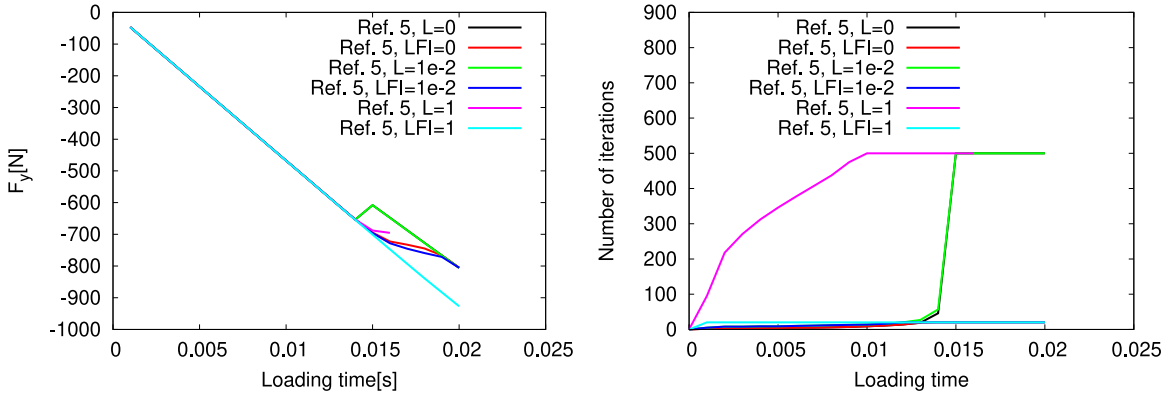

Fig. 23. Example 4: Comparison of the forces (left) over the top boundary and the number iterations on the finest refinement level for various iterations and choices of stabilization parameters L. As observed in Fig. 20, the choice of $L = 1$ is not recommended because the influence on the physical model is too high and therefore, the numerical solution is wrong; namely the crack starts propagating much later than for smaller L.

but this is expected since we use $\varepsilon = 2h$, and as our analysis demonstrates, the convergence rate is dependent on ε. The variation in iteration numbers with mesh refinement is in any case sufficiently small enough that we conclude our algorithm is robust with respect to mesh refinement.

Moreover, due to the iteration spikes at the critical loading steps, we have included, for comparison, several results in which the iteration has been truncated (labeled LFI in Examples 1–4). Due to the monotonic convergence of the scheme, this strategy still produces acceptable results, while effectively avoiding the iteration spikes. We therefore conclude, at least for the particular examples presented here, that a truncation of the L-scheme can be employed for greatly improved efficiency with only negligible (depending on the situation at hand, of course) loss of accuracy.

Acknowledgments

This work forms part of Research Council of Norway project 250223. The authors also acknowledges the support from the University of Bergen, Norway. The first author, MKB, thanks the group 'Wissenschaftliches Rechnen' of the Institute of Applied Mathematics of the Leibniz University Hannover for the hospitality during his research stay from Oct–Dec 2018. The second author, TW, has been supported by the German Research Foundation, Priority Program 1748 (DFG SPP 1748) named *Reliable Simulation Techniques in Solid Mechanics. Development of Non-standard Discretization Methods, Mechanical and Mathematical Analysis*. The subproject within the SPP1748 reads *Structure Preserving Adaptive Enriched Galerkin Methods for Pressure-Driven 3D Fracture Phase-Field Models* (WI 4367/2-1).

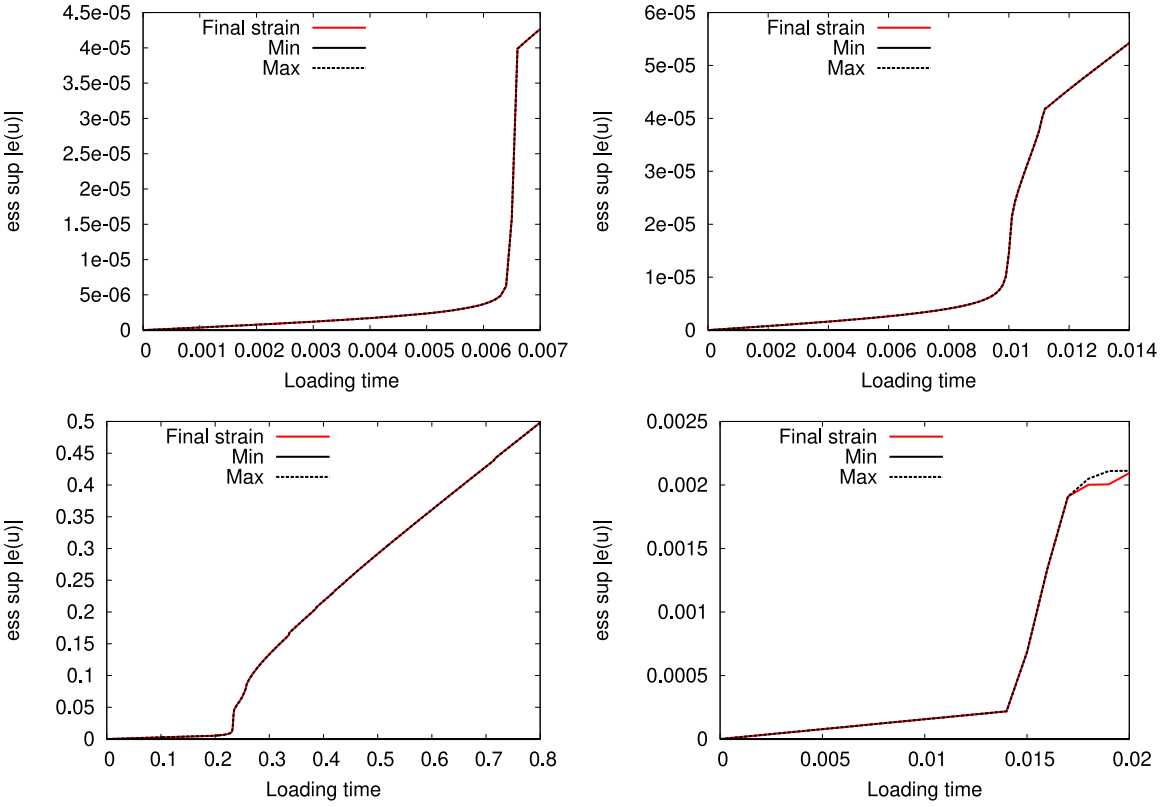

Fig. 24. All Examples 1, 2, 3, 4: Comparison of $\operatorname{ess\,sup}_{x\in B} |\mathbf{e}(u^n(x))|$ and the minimal/maximal $\operatorname{ess\,sup}_{x\in B} |\mathbf{e}(u^n(x))|$ per loading time step.

References

[1] A.A. Griffith, M. Eng, Vi. the phenomena of rupture and flow in solids, Philos. Trans. R. Soc. Lond. A Math. Phys. Eng. Sci. 221 (582–593) (1921) 163–198.

[2] B. Bourdin, G. Francfort, J.-J. Marigo, Numerical experiments in revisited brittle fracture, J. Mech. Phys. Solids 48 (4) (2000) 797–826.

[3] G.A. Francfort, J.-J. Marigo, Revisiting brittle fracture as an energy minimization problem, J. Mech. Phys. Solids 46 (8) (1998) 1319–1342, http://dx.doi.org/10.1016/S0022-5096(98)00034-9.

[4] T. Gerasimov, L.D. Lorenzis, A line search assisted monolithic approach for phase-field computing of brittle fracture, Comput. Methods Appl. Mech. Engrg. 312 (2016) 276–303.

[5] A. Mesgarnejad, B. Bourdin, M. Khonsari, Validation simulations for the variational approach to fracture, Comput. Methods Appl. Mech. Engrg. 290 (2015) 420–437.

[6] T. Wick, An error-oriented Newton/inexact augmented Lagrangian approach for fully monolithic phase-field fracture propagation, SIAM J. Sci. Comput. 39 (4) (2017) B589–B617, http://dx.doi.org/10.1137/16M1063873.

[7] T. Wick, Modified Newton methods for solving fully monolithic phase-field quasi-static brittle fracture propagation, Comput. Methods Appl. Mech. Engrg. 325 (2017) 577–611, http://dx.doi.org/10.1016/j.cma.2017.07.026.

[8] B. Bourdin, Numerical implementation of the variational formulation for quasi-static brittle fracture, Interfaces Free Bound. 9 (2007) 411–430.

[9] B. Bourdin, G. Francfort, J.-J. Marigo, The variational approach to fracture, J. Elasticity 91 (1–3) (2008) 1–148.

[10] S. Burke, C. Ortner, E. Süli, An adaptive finite element approximation of a variational model of brittle fracture, SIAM J. Numer. Anal. 48 (3) (2010) 980–1012.

[11] C. Miehe, M. Hofacker, F. Welschinger, A phase field model for rate-independent crack propagation: robust algorithmic implementation based on operator splits, Comput. Methods Appl. Mech. Engrg. 199 (45–48) (2010) 2765–2778, http://dx.doi.org/10.1016/j.cma.2010.04.011.

[12] T. Heister, M.F. Wheeler, T. Wick, A primal-dual active set method and predictor-corrector mesh adaptivity for computing fracture propagation using a phase-field approach, Comput. Methods Appl. Mech. Engrg. 290 (2015) 466–495.

[13] N. Castelletto, J. White, H. Tchelepi, Accuracy and convergence properties of the fixed-stress iterative solution of two-way coupled poromechanics, Int. J. Numer. Anal. Methods Geomech. 39 (14) (2015) 1593–1618.

[14] J. Kim, H.A. Tchelepi, R. Juanes, et al., Stability, accuracy and efficiency of sequential methods for coupled flow and geomechanics, in: SPE Reservoir Simulation Symposium, Society of Petroleum Engineers, 2009.
[15] A. Mikelić, B. Wang, M.F. Wheeler, Numerical convergence study of iterative coupling for coupled flow and geomechanics, Comput. Geosci. 18 (3–4) (2014) 325–341, http://dx.doi.org/10.1007/s10596-013-9393-8.
[16] A. Mikelić, M.F. Wheeler, Convergence of iterative coupling for coupled flow and geomechanics, Comput. Geosci. 17 (3) (2013) 455–461, http://dx.doi.org/10.1007/s10596-012-9318-y.
[17] F. List, F.A. Radu, A study on iterative methods for solving Richards' equation, Comput. Geosci. 20 (2) (2016) 341–353, http://dx.doi.org/10.1007/s10596-016-9566-3.
[18] I.S. Pop, F. Radu, P. Knabner, Mixed finite elements for the Richards' equation: linearization procedure, J. Comput. Appl. Math. 168 (1–2) (2004) 365–373, http://dx.doi.org/10.1016/j.cam.2003.04.008.
[19] M. Borregales, F.A. Radu, K. Kumar, J.M. Nordbotten, Robust iterative schemes for non-linear poromechanics, Comput. Geosci. 22 (4) (2018) 1021–1038, http://dx.doi.org/10.1007/s10596-018-9736-6.
[20] J.W. Both, M. Borregales, J.M. Nordbotten, K. Kumar, F.A. Radu, Robust fixed stress splitting for Biot's equations in heterogeneous media, Appl. Math. Lett. 68 (2017) 101–108, http://dx.doi.org/10.1016/j.aml.2016.12.019.
[21] M. Kirkesæther Brun, E. Ahmed, I. Berre, J.M. Nordbotten, F.A. Radu, Monolithic and splitting based solution schemes for fully coupled quasi-static thermo-poroelasticity with nonlinear convective transport, 2019, arXiv e-prints, arXiv:1902.05783.
[22] L.C. Evans, Partial Differential Equations, second ed., in: Graduate Studies in Mathematics, vol. 19, American Mathematical Society, Providence, RI, 2010, p. xxii+749.
[23] K. Yosida, Functional Analysis, in: Classics in Mathematics, Springer-Verlag, Berlin, 1995, p. xii+501, http://dx.doi.org/10.1007/978-3-642-61859-8, Reprint of the sixth (1980) edition.
[24] D. Cioranescu, P. Donato, An introduction to homogenization, in: Oxford Lecture Series in Mathematics and its Applications, vol. 17, The Clarendon Press, Oxford University Press, New York, 1999, p. x+262.
[25] G.H. Hardy, J.E. Littlewood, G. Pólya, Inequalities, in: Cambridge Mathematical Library Series, Cambridge University Press, 1967.
[26] J.M. Sargado, E. Keilegavlen, I. Berre, J.M. Nordbotten, High-accuracy phase-field models for brittle fracture based on a new family of degradation functions, J. Mech. Phys. Solids 111 (2018) 458–489, http://dx.doi.org/10.1016/j.jmps.2017.10.015.
[27] I. Neitzel, T. Wick, W. Wollner, An optimal control problem governed by a regularized phase-field fracture propagation model, SIAM J. Control Optim. 55 (4) (2017) 2271–2288, http://dx.doi.org/10.1137/16M1062375.
[28] A. Mikelić, M.F. Wheeler, T. Wick, A quasi-static phase-field approach to pressurized fractures, Nonlinearity 28 (5) (2015) 1371–1399.
[29] A. Mikelić, M.F. Wheeler, T. Wick, Phase-field modeling through iterative splitting of hydraulic fractures in a poroelastic medium, GEM - Int. J. Geomath. 10 (1) (2019).
[30] W. Cheney, Analysis for Applied Mathematics, in: Graduate Texts in Mathematics, vol. 208, Springer-Verlag, New York, 2001, p. viii+444, http://dx.doi.org/10.1007/978-1-4757-3559-8.
[31] S. Sun, B. Rivière, M.F. Wheeler, A combined mixed finite element and discontinuous Galerkin method for miscible displacement problem in porous media, in: Recent Progress in Computational and Applied PDES (Zhangjiajie, 2001), Kluwer/Plenum, New York, 2002, pp. 323–351.
[32] S. Sun, M.F. Wheeler, Discontinuous Galerkin methods for coupled flow and reactive transport problems, Appl. Numer. Math. 52 (2–3) (2005) 273–298, http://dx.doi.org/10.1016/j.apnum.2004.08.035.
[33] L. Ambrosio, V.M. Tortorelli, Approximation of functionals depending on jumps by elliptic functionals via Γ-convergence, Comm. Pure Appl. Math. 43 (1990) 999–1036.
[34] L. Ambrosio, V.M. Tortorelli, On the approximation of free discontinuity problems, Boll. Unione Mat. Ital. B 6 (1992) 105–123.
[35] J. Nocedal, S.J. Wright, Numerical Optimization, Springer Ser. Oper. Res. Financial Engrg., 2006.
[36] M. Fortin, R. Glowinski, Augmented Lagrangian Methods: Applications to the Numerical Solution of Boundary Value Problems, in: Stud. Math. Appl. 15, North Holland, Amsterdam, 1983.
[37] R. Glowinski, P.L. Tallec, Augmented Lagrangian and Operator-Splitting Methods in Nonlinear Mechanics, in: SIAM Stud. Appl. Math. 9, SIAM, Philadelphia, 1989.
[38] M.F. Wheeler, T. Wick, W. Wollner, An augmented-lagangrian method for the phase-field approach for pressurized fractures, Comput. Methods Appl. Mech. Engrg. 271 (2014) 69–85.
[39] K. Mang, T. Wick, Numerical methods for variational phase-field fracture problems, Institutionelles Repositorium der Leibniz Universität Hannover, Hannover, 2019, http://dx.doi.org/10.15488/5129.
[40] T. Gerasimov, L.D. Lorenzis, On penalization in variational phase-field models of brittle fracture, Comput. Methods Appl. Mech. Engrg. 354 (2019) 990–1026.
[41] C. Miehe, F. Welschinger, M. Hofacker, Thermodynamically consistent phase-field models of fracture: variational principles and multi-field fe implementations, Int. J. Numer. Methods Engrg. 83 (2010) 1273–1311.
[42] H. Amor, J.-J. Marigo, C. Maurini, Regularized formulation of the variational brittle fracture with unilateral contact: Numerical experiments, J. Mech. Phys. Solids 57 (2009) 1209–1229.
[43] P. Deuflhard, Newton Methods for Nonlinear Problems, in: Springer Series in Computational Mathematics, vol. 35, Springer Berlin Heidelberg, 2011.
[44] T.A. Davis, I.S. Duff, An unsymmetric-pattern multifrontal method for sparse LU factorization, SIAM J. Matrix Anal. Appl. 18 (1) (1997) 140–158.
[45] D. Arndt, W. Bangerth, D. Davydov, T. Heister, L. Heltai, M. Kronbichler, M. Maier, J.-P. Pelteret, B. Turcksin, D. Wells, The deal.II library, version 8.5, J. Numer. Math. (2017) http://dx.doi.org/10.1515/jnma-2016-1045.
[46] W. Bangerth, R. Hartmann, G. Kanschat, deal.II – a general purpose object oriented finite element library, ACM Trans. Math. Software 33 (4) (2007) 24/1–24/27.

[47] T. Wick, Solving monolithic fluid-structure interaction problems in arbitrary Lagrangian Eulerian coordinates with the deal.II library, Arch. Numer. Softw. 1 (2013) 1–19.
[48] M. Ambati, T. Gerasimov, L. De Lorenzis, A review on phase-field models of brittle fracture and a new fast hybrid formulation, Comput. Mech. 55 (2) (2015) 383–405.
[49] B. Winkler, Traglastuntersuchungen von Unbewehrten und Bewehrten Betonstrukturen auf der Grundlage Eines Objektiven Werkstoffgesetzes fuer Beton (PhD thesis), University of Innsbruck, 2001.
[50] K. Mang, T. Wick, W. Wollner, A phase-field model for fractures in nearly incompressible solids, Comput. Mech. (2019) http://dx.doi.org/10.1007/s00466-019-01752-w.
[51] T.N. Bittencourt, P.A. Wawrzynek, A.R. Ingraffea, J.L. Sousa, Quasi-automatic simulation of crack propagation for 2d lefm problems, Eng. Fract. Mech. 55 (2) (1996) 321–334.